

Simultaneous geometric calibration and orbit-attitude determination of Hayabusa2's deployable camera (DCAM3)

Shota Kikuchi^{a,*}, Kei Shirai^b, Ko Ishibashi^c, Koji Wada^c, Yasuhiro Yokota^d, Rie Honda^{e,1},
Toshihiko Kadono^f, Yuri Shimaki^d, Naoya Sakatani^d, Kazunori Ogawa^d,
Hirotaka Sawada^d, Takanao Saiki^d, Yuya Mimasu^d, Yuto Takei^d, Seiji Sugita^{g,c},
Toru Kouyama^h, Naru Hirataⁱ, Satoru Nakazawa^d, Makoto Yoshikawa^d, Satoshi Tanaka^d,
Sei-ichiro Watanabe^j, Yuichi Tsuda^d, Masahiko Arakawa^b

^a National Astronomical Observatory of Japan, Mitaka, Tokyo 181-8588, Japan

^b Kobe University, Kobe 657-8501, Japan

^c Planetary Exploration Research Center, Chiba Institute of Technology, Narashino 275-0016, Japan

^d Japan Aerospace Exploration Agency, Sagamihara 252-5210, Japan

^e Ehime University, Matsuyama 790-8577, Japan

^f University of Occupational and Environmental Health, Kitakyushu 807-8555, Japan

^g The University of Tokyo, Tokyo 113-0033, Japan

^h National Institute of Advanced Industrial Science and Technology, Tokyo 135-0064, Japan

ⁱ The University of Aizu, Aizu-Wakamatsu 965-8580, Japan

^j Nagoya University, Nagoya 464-8601, Japan

Received 27 February 2024; received in revised form 8 April 2024; accepted 28 April 2024

Available online 3 May 2024

Abstract

Hayabusa2's deployable camera (DCAM3) was deployed from the spacecraft near the asteroid Ryugu to successfully monitor the artificial cratering experiment. Scientific analyses of the observed impact ejecta require accurate determination of the camera's position and orientation. However, in contrast to conventional spacecraft operations, DCAM3 lacked the capability to acquire orbit tracking data and attitude sensor data due to its limited onboard resources. Even though the optical images obtained by DCAM3 itself are the only source of geometric information, they were subject to significant distortion caused by the rolling shutter effect and lens distortion. This research is, therefore, designed to simultaneously estimate the image distortion and the orbital and attitude motions of DCAM3, relying solely on its image data. The relative geometry between the camera and the asteroid is reconstructed from the geographic information of the observed feature points by incorporating distortion effects. The proposed method involves segmenting the geometry reconstruction, with more than ten thousand feature measurements, into smaller-scale least-squares problems. The image-based estimation yields consistent distortion, orbit, and attitude solutions with pixel-scale accuracy. The analysis results indicate that DCAM3 experienced significant nutation of its optical axis during ballistic flight in a semi-elliptical orbit. In addition, these motions were sensitive enough to simultaneously determine system parameters, such as the gravitational parameter of Ryugu and the inertia moment of DCAM3. This paper illustrates the potential of deployable camera systems as a promising option for enhancing the scientific and engineering aspects of asteroid exploration.

© 2024 COSPAR. Published by Elsevier B.V. This is an open access article under the CC BY license (<http://creativecommons.org/licenses/by/4.0/>).

Keywords: Asteroid exploration; Optical navigation; Image calibration; Small satellite; Gravimetry

* Corresponding author.

E-mail address: shota.kikuchi@nao.ac.jp (S. Kikuchi).

¹ Deceased.

1. Introduction

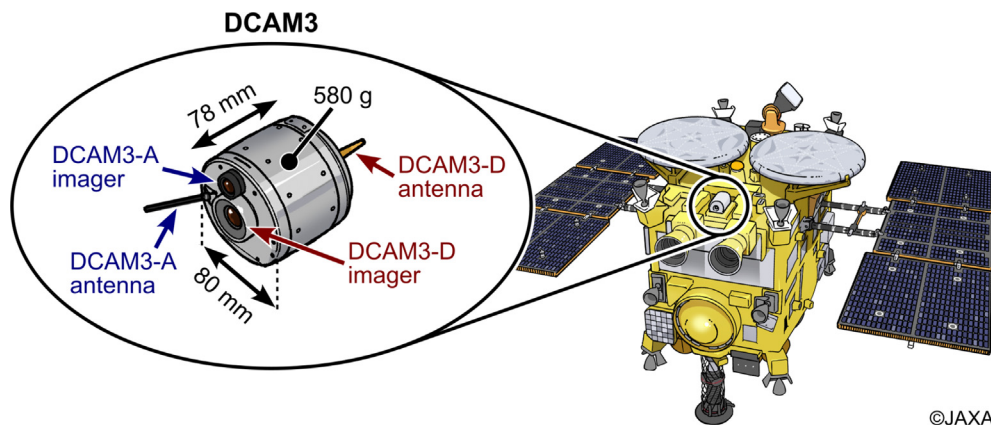
Piggyback payloads have demonstrated immense value in deep space exploration. In particular, the low-gravity environment around small bodies, including asteroids and comets, harnesses the full potential of small-scale spacecraft with limited onboard resources. Several small-body missions employed deployable payloads as secondary spacecraft to accomplish challenging tasks that were too risky or even impossible for the primary spacecraft. Examples include Philae in the Rosetta mission to comet 67P/Churyumov–Gerasimenko (Bibring et al., 2007) and MAS-COT and MINERVA-III in the Hayabusa2 mission to asteroid Ryugu (Ho et al., 2017; Yoshimitsu et al., 2019). These landers and rovers were delivered to the surfaces of their target bodies for in situ observation. The DART spacecraft also carried a small secondary spacecraft called LICIACube (Dotto et al., 2021). This CubeSat was designed to observe the consequences of the DART impact on asteroid Dimorphos during its flyby.

Another successful example is the deployable camera (DCAM3) installed on Hayabusa2, as illustrated in Fig. 1, for the impact experiment on Ryugu (Sawada et al., 2017). In this operation, a small carry-on impactor (SCI) detached from Hayabusa2 autonomously detonated itself and fired a projectile toward the asteroid surface (Arakawa et al., 2020; Saiki et al., 2020). The Hayabusa2 spacecraft moved to the opposite side of the SCI target point to avoid impact ejecta and SCI debris, as sketched in Fig. 2. Hence, DCAM3 took place of Hayabusa2 to monitor the impact event, yielding valuable scientific data for the characterization of artificial cratering (Kadono et al., 2020; Wada et al., 2021). As is the norm in optical observations, accurate interpretation of image data necessitates precise geometric information on observation conditions and image calibration. However, acquiring these fundamental data is not a straightforward endeavor for DCAM3, with a mass of only 0.58 kg.

The imaging geometry can be reconstructed through orbit and attitude determination, which were accomplished by combining multiple datasets for the aforementioned piggyback payloads other than DCAM3 (see Table 1). In the previous cases, the secondary spacecraft were either optically tracked by the primary spacecraft or radiometrically tracked by ground stations (Jurado et al., 2016; Scholten et al., 2019; Van Wal et al., 2019; Lubey et al., 2023). In contrast, neither of these options applied to the DCAM3 operation because DCAM3 was not optically visible from the retreating spacecraft and was not capable of communicating directly with Earth. In addition, DCAM3 was not equipped with any additional sensors that can independently obtain attitude information, such as gyro sensors, star trackers, sun sensors, and photoelectric cells (Heinisch et al., 2016; Garmier et al., 2021; Yoshimitsu and Kubota, 2020). For these reasons, the position and orientation of the camera must be estimated solely from optical images that captured Ryugu within its field of view.

What further complicates this situation is the significant image distortion caused by DCAM3's wide field of view and rapid spinning (Ishibashi et al., 2017). The in-flight geometric calibration necessitates information on viewing conditions determined by the camera's position and orientation. On the other hand, precise orbit and attitude estimation require geometrically corrected images. To address these interrelated issues, this research proposes image-based simultaneous geometric calibration and orbit-attitude determination. The geometric relationship between DCAM3 and Ryugu is reconstructed by correlating feature points captured in DCAM3 images and pre-existing points with known three-dimensional locations. Because the geometry estimation involves more than 10,000 feature point measurements, we devise a stepwise least-squares algorithm to address this large-scale problem with reasonable computational time and stability.

The uniqueness of the DCAM3 operation also lies in its orbital path. The previous secondary spacecraft listed in



©JAXA

Fig. 1. Illustration of DCAM3 onboard Hayabusa2. The camera consists of analog (DCAM3-A) and digital (DCAM3-D) systems. Illustration credit: JAXA.

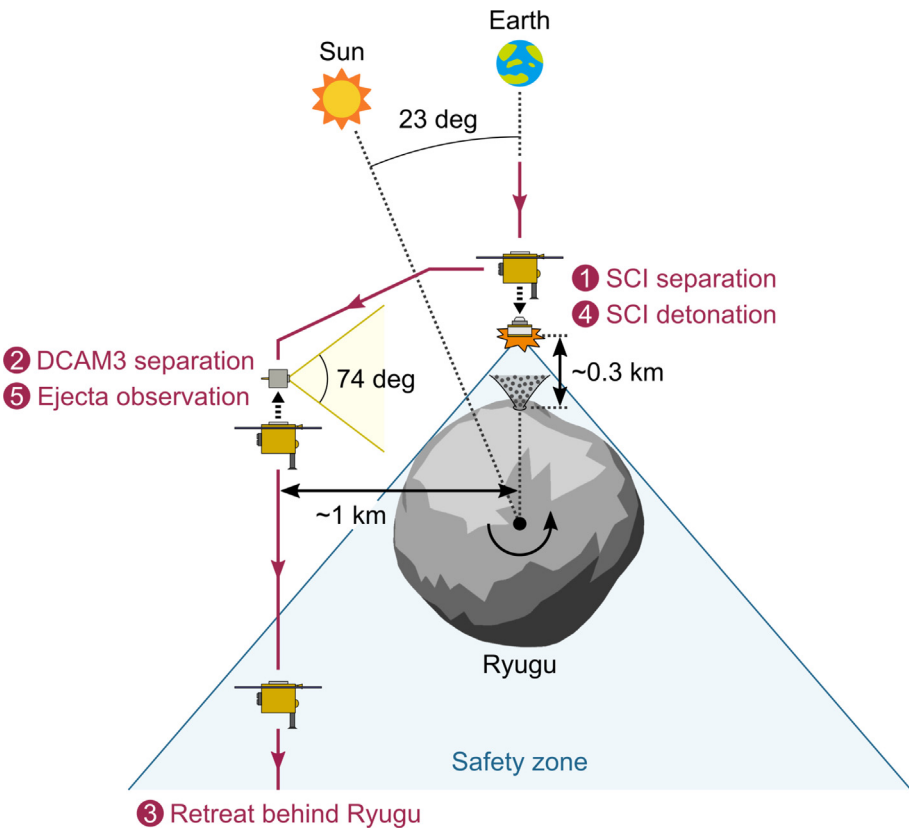


Fig. 2. Schematic illustration of the SCI-DCAM3 operation (Saiki et al., 2020). The Hayabusa2 trajectory sequence within the plane containing the sun, Earth, and Ryugu is sketched, which approximately corresponds to the view from the north pole of the asteroid.

Table 1
Piggyback payloads that accomplished remote-sensing observations of small bodies.

Mission	Payload	Mass	Trajectory	Orbit tracking		Attitude data [§]	References
				Optical [*]	Radiometric [†]		
Rosetta	Philae	98 kg	Landing	Yes	No	Yes	[1], [2]
Hayabusa2	MASCOT	9.6 kg	Landing	Yes	No	Yes	[3], [4]
	MINERVA-III	1.1–1.2 kg	Landing	Yes	No	Yes	[5], [6]
	DCAM3	0.58 kg	Suborbital	No	No	No	This study
DART	LICIACube	14 kg	Flyby	No	Yes	Yes	[7]

^{*}Optical tracking from the primary spacecraft.
[†]Radiometric tracking from ground stations.
[§]Information sources independent of observation cameras.
[1] Jurado et al. (2016). [2] Heinisch et al. (2016). [3] Scholten et al. (2019). [4] Garmier et al. (2021).
[5] Van Wal et al. (2019). [6] Yoshimitsu and Kubota (2020). [7] Luby et al. (2023)

Table 1 were specifically designed for either landing or flyby, and thus, their trajectories exhibited rectilinear motion relative to the target bodies. In contrast, DCAM3 experienced suborbital flight for more than 6 hr, resulting in orbital and attitude behaviors sensitive enough to their dynamical models. Therefore, the orbit and attitude determination of DCAM3 via the batch least-squares method involves estimations of dynamical system parameters, which include the gravitational parameter of Ryugu. As a byproduct of this research, we demonstrate purely optical gravimetry without relying on conventional radiometric or altimetric data.

Successful image undistortion and orbit and attitude estimation allow precise determination of the camera’s viewing geometry. Consequently, our work contributes to in-depth characterization of the evolution of SCI impact ejecta observed in DCAM3 images (Kikuchi et al., 2023). This research illustrates that even a subkilogram spacecraft could produce cutting-edge scientific results. The geometry reconstruction is also of engineering importance, serving as a performance evaluation of the DCAM3 system and operation. The key to the proposed approach lies in extracting dynamical information solely from optical images, which renders it suitable for any upcoming small-body

exploration. Previous studies posited the idea of using multiple tiny deployable spacecraft for remote-sensing observations, such as global mapping and gravimetry, of small bodies (Villa et al., 2021; Stacey et al., 2022). The CubeSats Milani and Juventas, installed on the Hera spacecraft, will function as orbiters for post-impact characterization of asteroids Didymos and Dimorphos (Ferrari et al., 2021; Goldberg et al., 2019). The demonstrated DCAM3 technology facilitates such advanced mission concepts, pushing the limits of deep space exploration.

This paper begins with an overview of the data and methods employed in this research. The associated mathematical foundation is provided in Section 3. The primary research results are detailed in Sections 4–6, which focus on image calibration, orbit determination, and attitude determination, respectively. Although these tasks are addressed in different sections, they were interrelated and thus were performed using the same dataset.

2. Data and methods

2.1. SCI-DCAM3 operation

This section provides an overview of the SCI experiment conducted in April 2019, including fundamental information for DCAM3 image analyses. The primary events including the separation of DCAM3 are illustrated in Fig. 2 (Saiki et al., 2020), and the event times are summarized in Table 2. Hayabusa2 approached Ryugu along the imaginary line connecting the asteroid and Earth. The spacecraft released SCI at a surface altitude of ~ 0.5 km (Saiki et al., 2020). The detached SCI activated a countdown timer to autonomously detonate itself after a predetermined period, during which the spacecraft was intended to escape.

Immediately after the SCI separation, several impulsive thrusting maneuvers were executed, guiding the spacecraft to the DCAM3 release point. DCAM3 was detached by a spring mechanism, which exerted torque to stabilize the camera attitude (Sawada et al., 2017). The distance between the separation point and the expected SCI impact point near the equator was ~ 1 km (Kikuchi et al., 2022), which is approximately double the asteroid radius. Then, the spacecraft retreated behind the asteroid to avoid debris

generated by the SCI detonation and impact cratering. SCI detonated 40 min after separation, accelerating a 2-kg projectile to a velocity of 2 km/s. The detonation altitude was estimated to be ~ 0.3 km from the asteroid surface (Saiki et al., 2020). The observation sequence of DCAM3 commenced 205 s prior to the SCI impact and lasted for at least 3 h. The evolution of impact ejecta was successfully captured within DCAM3 images (Wada et al., 2021; Kadono et al., 2020).

2.2. DCAM3 specification

The DCAM3 technology follows that of DCAM1 and DCAM2, which were installed on the solar sail IKAROS (Sawada et al., 2011; Tsuda et al., 2011). The purpose of DCAM1 and DCAM2 was to confirm the deployment of the sail membrane and observe its deformation as an engineering mission. Their successor, DCAM3, was redesigned to maximize the scientific outcomes of the SCI experiment, enabling in situ observation of ejecta plume evolution. DCAM5 was subsequently proposed as an advanced concept for applying the deployable camera technology to the exploration of small-body surfaces (Çelik et al., 2019).

Primary DCAM3 specifications pertinent to this research are summarized in Table 3. Fig. 1 shows that DCAM3 had a cylindrical shape with a height of 78 mm and a diameter of 80 mm (Sawada et al., 2017). DCAM3 had a mass of 0.58 kg and thus is categorized as a picosatellite in conventional small-satellite taxonomy (Janson, 2011). The camera was powered by primary batteries, ensuring a minimum observation time of 2 hr (Ogawa et al., 2017). DCAM3 was equipped with two independent optical and communication systems, namely, DCAM3-A (analog) and DCAM3-D (digital), as illustrated in Fig. 1. The digital system was specifically designed for high-resolution scientific observations. Therefore, only DCAM3-D images are used in our analyses, and those images are simply referred to as DCAM3 images hereafter.

The DCAM3-D sensor had a wide field-of-view angle of approximately 74 deg. The imaging system was capable of generating square images with $2000 \text{ px} \times 2000 \text{ px}$. The pixel resolution at the center of the field of view was 0.615 mrad/px (Ishibashi et al., 2017), corresponding to a spatial resolution of $\sim 0.6 \text{ m/px}$ at a typical observation

Table 2

Primary events during the SCI-DCAM3 operation. Event epochs are shown in Coordinated Universal Time (UTC) and as relative time from the DCAM3 separation.

Epoch (UTC)	Relative time	Event
5 April 2019	01:56:11	SCI separation
	02:14:25	DCAM3 separation
	02:32:45	DCAM3 observation start
	02:36:10	SCI detonation
	05:41:06	DCAM3 observation end*
	08:34:34	DCAM3 impact on the asteroid†

*The latest epoch at which a valid image was acquired.

†Estimated from the reconstructed trajectory with an uncertainty of ~ 10 min.

Table 3
Primary mechanical and optical properties of DCAM3 (Sawada et al., 2017; Ogawa et al., 2017; Ishibashi et al., 2017).

Category	Item	Value
Mechanical properties	Mass	0.58 kg
	Height	78 mm
	Diameter	80 mm
Optical properties	Field of view	74 deg
	Number of pixels	2000 × 2000
	Pixel resolution	0.615 mrad/px
	Observation frequency	0.01–1 Hz

distance of 1 km. The minimum time interval for observations was 1 s, which was extended to approximately 100 s in later observations to reduce the total data size. For the same purpose, some of the images were binned to 500 px × 500 px in the onboard system. The detailed timetable of DCAM3 observations is presented in Ogawa et al. (2017).

The optical system of DCAM3-D employed an electronic rolling shutter (Ishibashi et al., 2017). This type of sensor sequentially records an image line by line, as opposed to capturing the entire image instantaneously. Due to the rapid rotation of DCAM3, the camera orientation shifted during the exposure of each individual pixel. This resulted in image distortion, a phenomenon hereafter termed the rolling shutter effect. Consequently, the distor-

tion profile was dependent on the attitude state of DCAM3 and thereby varied over time.

2.3. Image data

Our DCAM3 image analysis involves feature point matching with reference images obtained by the Hayabusa2 telescopic optical navigation camera (ONC-T). A schematic illustration of the proposed algorithm is shown in Fig. 3. This section provides an overview of the DCAM3 and ONC-T images used in this paper.

2.3.1. DCAM3 images

DCAM3 obtained and downlinked a total of 1,422 valid images. Because of the camera’s nutation, Ryugu was captured in only a subset of the images. Fig. 4 shows the pixel areas of the asteroid observed in DCAM3 images. Raw images without geometric calibration are used in this analysis. The ratio of the pixel area occupied by the asteroid is approximately 28% at maximum. The pixel area varies significantly even at almost the same epochs due to the drastic changes in the orientation of the optical axis. In addition, the profile exhibits gradual decay, and the pixel area diminishes to zero at ~ 200 min after DCAM3 separation. This is due to the optimization of the initial attitude, which was specifically aimed at monitoring the impact phenom-

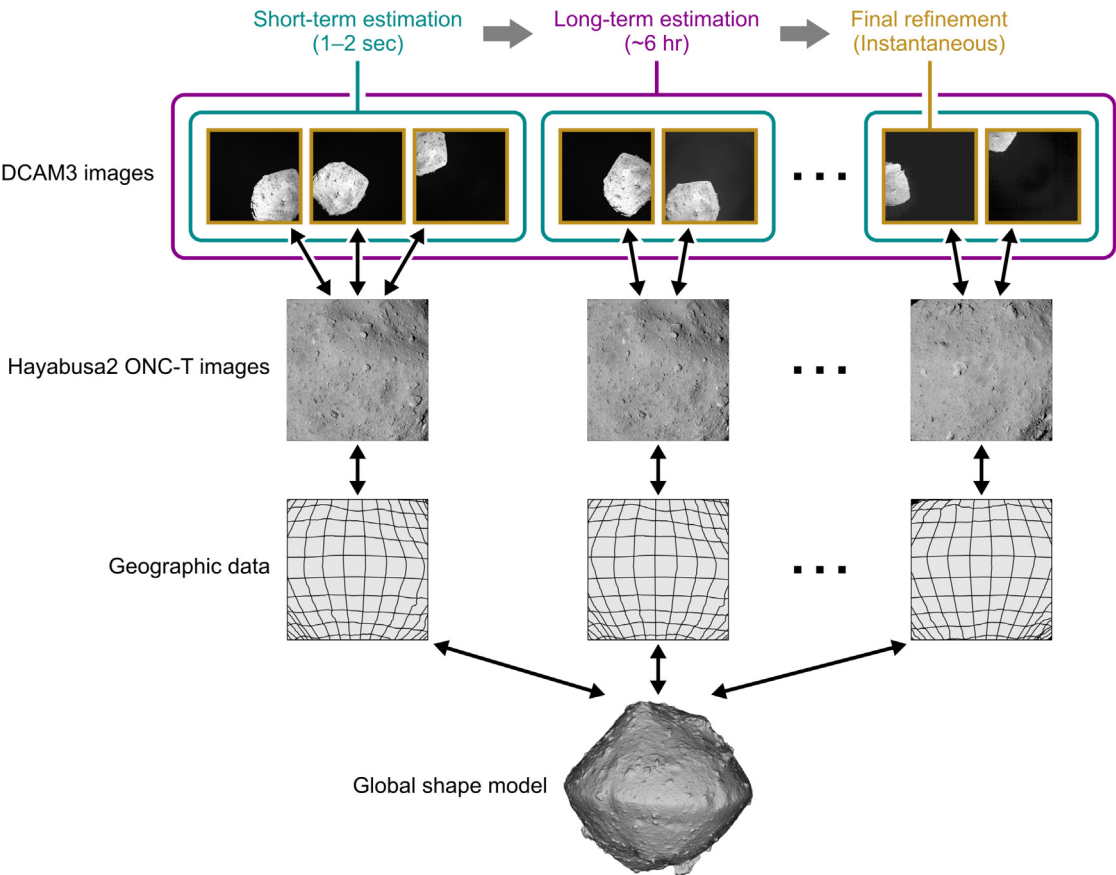


Fig. 3. Schematic diagram of the analysis process. The parameters estimated in each step are summarized in Table 4.

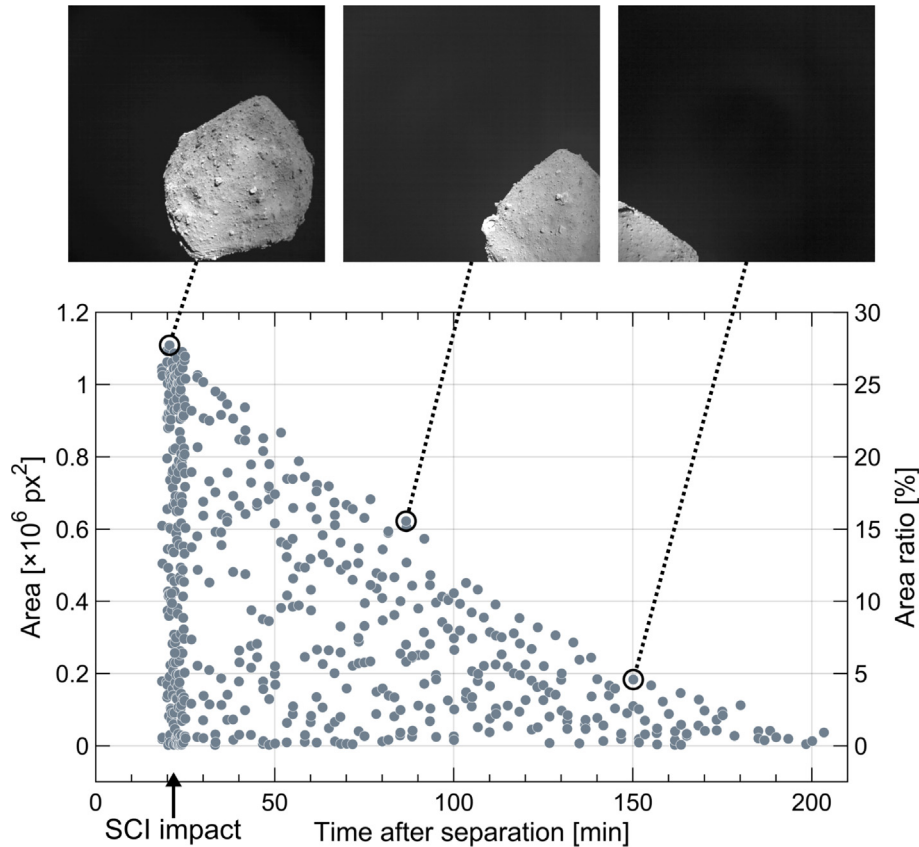


Fig. 4. Time history of the pixel area of Ryugu captured in a DCAM3 image. The left and right vertical axes indicate the pixel area and its ratio to the total number of pixels, respectively. The top three panels display examples of DCAM3 images, which correspond to the encircled dots. The sizes of the binned images are adjusted to match the sizes of the original images.

ena at the beginning of the imaging sequence. The camera obtained images with a cadence of 1 s near the time of the SCI detonation, while the frequency was reduced to intervals of ~ 100 s at later epochs (Ogawa et al., 2017). The former and latter are referred to as high- and low-frequency observations, respectively.

The geometric calibration and state estimation proposed in this study rely on feature point matching; thus, the asteroid must be captured within a sufficiently large pixel area. The scope of our analysis is, therefore, confined to the first 90 min after the DCAM3 separation. Within this time range, DCAM3 images that have pixel area ratios larger than approximately 5% are fed into the image analysis process. Consequently, this study used a total of 245 DCAM3 images, which included 109 full-size images and 136 binned images. In the data presentation of this paper, the pixel values of the binned images are altered to match those of the full-size images. A list of those images is provided in the supplementary file.

2.3.2. Hayabusa2 ONC-T images

ONC-T has a field of view of 6.27 deg and a resolution of $1024\text{px} \times 1024\text{px}$ (Kameda et al., 2017). We use eight ONC-T images as reference images to extract geometric

information from DCAM3 images. These reference data were acquired during the mid-altitude operation conducted by Hayabusa2 in August 2018 (Tsuda et al., 2020). The nadir surface altitudes during the observations were approximately 5 km. This altitude corresponds to a spatial resolution of 0.5–0.6 m/px, which is roughly comparable to that of full-size DCAM3 images.

The calibrated ONC-T images are available at the PDS4 archive (Suzuki et al., 2018; Sugita et al., 2022). The ancillary geographic data of the reference ONC-T images are also used to locate matched feature points in DCAM3 images (see Fig. 3). The ONC-T dataset contains information on latitudinal and longitudinal coordinates for each pixel, from which the three-dimensional positions of the observed surface points are calculated. Further details regarding the reference ONC-T images are provided in the supplementary material.

2.4. Shape model

The latitude and longitude of arbitrary surface points are converted to three-dimensional asteroid-fixed coordinates based on a global shape model of Ryugu. The adopted polyhedral shape model, which is shown in the

bottom part of Fig. 3, consists of three million triangular facets. This model was developed via the structure-from-motion (SFM) method (Watanabe et al., 2019) and is identified as version v20200815. In addition to the localization of feature points, the global shape model is used to create simulated DCAM3 images for validation and to compute the dispersion of the DCAM3 landing points.

Another application of the global shape model is the calculation of the asteroid gravity field. As described in Section 3.2, the orbital motion of DCAM3 is propagated by accounting for higher-order gravitational effects. The spherical harmonic coefficients are computed from the v20180804 version of the SFM global model. For this purpose, a reduced version with 786,432 facets is adopted to minimize the computational cost. The difference in model versions is negligible because of the limited effect of higher-order gravitational terms, as discussed in Section 5.1.

2.5. Analysis workflow

The cumulative total number of feature points identified for the geometry reconstruction is greater than 10,000. It is unrealistic to solve the consistent solution set of distortion, orbit, and attitude in a single process from such a vast array of measurements, in terms of computational cost and numerical stability. Therefore, we develop a stepwise algorithm to address this large-scale optimization problem. The proposed method consists of three main processes, as shown in Fig. 3: short-term estimation, long-term estimation, and final refinement. The parameters estimated in each analysis are summarized in Table 4. The following subsections are devoted to the analysis workflow, while its mathematical foundation is presented later in Section 3.

2.5.1. Short-term estimation

Instead of immediately processing all DCAM3 images at once, the analysis begins by segmenting the geometry estimation into shorter periods. In this initial phase, the relative geometry between DCAM3 and Ryugu is numerically estimated from two or three consecutive images with time intervals of 1 s. The task is similar to

the perspective-n-point problem in that the position and orientation of the camera relative to the subject are estimated from multiple three-dimensional reference points (Fischler and Bolles, 1981). However, we also determine the angular velocity of DCAM3 in this short-term estimation because its attitude exhibited drastic changes even within the short spans of 1–2 s.

The advantage of this approach is that the rolling shutter effect can be simultaneously modeled, which is a direct consequence of the camera's attitude motion. The lens distortion coefficients are also treated as estimation parameters. Hence, the combined distortion profile for each image is reconstructed in this process. The optimization of the entire scene geometry shares some commonality with the bundle adjustment in photogrammetry (Triggs et al., 2000), except that the shape of the observed asteroid is fixed in our case. The attitude motion is modeled as torque-free rotation and is numerically propagated. In contrast, the camera position is assumed to be fixed with respect to the asteroid-centered inertial frame given its negligible variations within a short duration. Table 4 lists the estimated, fixed, and excluded parameters in this phase.

2.5.2. Long-term estimation

The subsequent process is designed to obtain the single consistent solution of the orbit and attitude profiles of DCAM3 for the entire period of interest. The long-term estimation relies on discrete estimates of the position, attitude, and angular velocity obtained in the short-term analyses described above. Avoiding the direct use of thousands of feature points enhances computational efficiency. This task is equivalent to conventional orbit and attitude determination based on the batch least-squares method (Montenbruck and Gill, 2000).

Long-term estimation is sensitive to the dynamical model, facilitating the estimation of system parameters in addition to state parameters. For the attitude motion, the moment of inertia tensor of DCAM3 and the time-varying external torque are estimated along with the camera's attitude angle and angular velocity. Similarly, the orbit determination process can treat the gravitational parameter of Ryugu as an estimation parameter, serving as optical gravimetry.

Table 4

Three main analysis processes and the associated set of estimation parameters. The star markers represent the items used as final estimates.

Category	Parameter	Analysis type		
		Short-term estimation	Long-term estimation	Final refinement
State	Position	Estimated	Estimated☆	Fixed
	Velocity	Not considered	Estimated☆	Not considered
	Attitude angle	Estimated	Estimated	Estimated☆
	Angular velocity	Estimated	Estimated☆	Not considered
Distortion	Rolling shutter effect	Estimated	Estimated☆	Fixed
	Lens distortion	Estimated	Estimated☆	Fixed
System	Gravitational parameter	Not considered	Estimated☆	Not considered
	Inertia tensor	Fixed	Estimated☆	Not considered
	External torque	Not considered	Estimated☆	Not considered

Moreover, the profile of image distortion is refined for each observation epoch by taking overall consistency into account. The most likely set of lens distortion coefficients is estimated, while the rolling shutter effect is evaluated based on the continuous attitude profile. This information can be immediately used to geometrically calibrate DCAM3 images for further scientific analyses.

2.5.3. Final refinement

The last process is the refinement of the attitude data. Although the optimal continuous solution is obtained in the long-term estimation, the accuracy of the attitude estimates is not necessarily ideal. This is due to the limitations in the model fidelity of attitude motion itself. The reconstruction of the attitude profile that perfectly follows the dynamical model at the pixel scale of DCAM3 images entails fundamental difficulties. This issue is not of concern for a general comprehension of long-term attitude motion. However, higher geometric accuracy might be required for in-depth scientific image analyses, such as the shape estimation of the SCI ejecta curtain.

With this motivation, we implement a process for the final attitude refinement. As summarized in Table 4, the attitude angle of DCAM3 at each observation epoch is slightly corrected without considering any dynamics. The camera's position is fixed to the value obtained in the long-term orbit determination. The distortion models are also consistent with those derived in the previous process. Unlike short- and long-term estimations, attitude refinement focuses on instantaneous states and thus does not require multiple images.

3. Formulation

3.1. Coordinate frame

In this paper, the following four three-dimensional Cartesian coordinate systems are used to describe the orbital and attitude motion of DCAM3 with respect to Ryugu.

- Asteroid-fixed coordinate frame: The origin is at the center of Ryugu. The x -axis points toward the intersection of the equator and the prime meridian of the asteroid, the z -axis lies along the rotation axis of the asteroid, and the y -axis completes a right-handed Cartesian coordinate system. The shape model and geocentric latitude and longitude of the asteroid are expressed with respect to this coordinate frame. The axes of this coordinate system are represented by the subscript 'AF'.
- Asteroid-centered inertial coordinate frame: The origin is at the center of Ryugu. The directions of the coordinate axes are identical to those of the J2000 ecliptic frame. The axes of this coordinate system are represented by the subscript 'ACI'.
- Camera-fixed coordinate frame: The origin is at the center of DCAM3. The x - and y -axes are oriented to the right and downward, respectively, along the image

plane, and the z -axis is aligned with the optical axis. The difference between the center of mass and the center of projection of the camera is neglected, and they are approximated to coincide with the origin of this coordinate frame.

- Camera-centered inertial coordinate frame: The origin is at the center of DCAM3. The coordinate axes are inertially fixed and lie along the ideal orientations of the camera-fixed coordinate axes at the moment of DCAM3 separation. The quaternion defining the transformation from the J2000 equatorial frame to this frame is $[0.632867, 0.491886, -0.493338, 0.337853]$, where the fourth component corresponds to the rotation angle about the Euler axis. This coordinate system is employed to define the attitude angles of DCAM3.

3.2. Orbital motion

The radial distance of DCAM3 from the center of Ryugu is less than 1.5 km from separation to landing. In this region, the asteroid gravity is more predominant than gravitational forces of the sun and other planetary bodies (Kikuchi et al., 2020). Thus, the orbital motion of DCAM3 can be accurately modeled as a two-body problem incorporating the effect of solar radiation pressure (SRP) as follows (Scheeres, 2012):

$$\ddot{\mathbf{r}} + 2\boldsymbol{\Omega} \times \dot{\mathbf{r}} + \boldsymbol{\Omega} \times (\boldsymbol{\Omega} \times \mathbf{r}) = \mathbf{a}_g + \mathbf{a}_p, \quad (1)$$

where \mathbf{r} is the position vector of DCAM3 with respect to the center of the asteroid, $\boldsymbol{\Omega}$ is the angular velocity vector of the asteroid rotation, and \mathbf{a}_g and \mathbf{a}_p are the accelerations due to the asteroid gravity and SRP, respectively.

The gravitational acceleration can be expressed as

$$\mathbf{a}_g = -\frac{\partial U}{\partial \mathbf{r}}, \quad (2)$$

where U denotes the gravitational potential of the asteroid. The potential is given by the following equation using spherical coordinates, where r , δ , and λ are the radial distance, geocentric latitude, and geocentric longitude, respectively (Kaula, 1966):

$$U = \frac{GM}{r} \sum_{j=0}^{n_g} \sum_{k=0}^j \left(\frac{R}{r}\right)^j P_{jk}(\sin \delta) \times (C_{jk} \cos k\lambda + S_{jk} \sin k\lambda). \quad (3)$$

Here, GM and R are the asteroid's standard gravitational parameter and reference radius, respectively, P_{jk} is the Legendre polynomial, C_{jk} and S_{jk} are the Stokes coefficients, and n_g is the maximum degree and order of the spherical harmonics. In this study, we derived the coefficients C_{jk} and S_{jk} from the shape model described in Section 2.4, assuming a constant-density polyhedron with a representative radius of $R = 526$ m (Werner, 1997). The gravity field is computed up to $n_g = 10$. While C_{jk} and S_{jk}

are fixed throughout the paper, GM is treated as an estimation parameter.

The SRP force is computed by modeling DCAM3 as a cylinder. Let us assume that solar photons impinge on ideal Lambertian surfaces without any transmission or reradiation, which is one of the simplest models for solar sail dynamics (McInnes, 1999; Scheeres, 2012). Then, the net SRP acceleration acting on the top and lateral surfaces of a cylinder is given by the equation below (see the Appendix for derivation).

$$\mathbf{a}_p = -\frac{\Phi dh}{m} \times \{(\mu_s C_s + \mu_d C_d + \mu_a C_a) \mathbf{s} + (v_s C_s + v_d C_d)(\mathbf{s} \cdot \hat{\mathbf{z}}) \hat{\mathbf{z}}\}, \quad (4)$$

where Φ is the magnitude of the SRP, which is a function of the solar distance; m , d , and h are the mass, diameter, and height of the cylinder, respectively; \mathbf{s} is a unit vector pointing from the cylinder to the sun; $\hat{\mathbf{z}}$ is a unit vector normal to the top surface of the cylinder; and C_s , C_d , and C_a are the optical constants representing the ratios of specular reflection, diffuse reflection, and absorption, respectively, the sum of which is equal to unity. The parameters μ_s , μ_d , μ_a , v_s , and v_d are nondimensional coefficients defined by the following equations:

$$\mu_s = \frac{4}{3} \sin \alpha, \quad (5a)$$

$$\mu_d = \frac{\pi d}{4 h} |\cos \alpha| + \sin \alpha + \frac{\pi}{6}, \quad (5b)$$

$$\mu_a = \frac{\pi d}{4 h} |\cos \alpha| + \sin \alpha, \quad (5c)$$

$$v_s = \frac{\pi d}{2 h} |\cos \alpha| - \frac{4}{3} \sin \alpha, \quad (5d)$$

$$v_d = \frac{\pi}{6} \left(\frac{d}{h} - 1 \right), \quad (5e)$$

where $\alpha \equiv \cos^{-1}(\mathbf{s} \cdot \hat{\mathbf{z}})$ denotes the solar angle. The solar radiation is incident from the $+z$ direction of the camera-fixed frame when $\cos \alpha > 0$ and from the $-z$ direction when $\cos \alpha < 0$.

Based on the specifications of DCAM3 shown in Section 2.2, $m = 0.58$ kg, $d = 80$ mm, and $h = 78$ mm. Considering the surface properties of aluminum, we set the optical constants to $C_s = 0.375$, $C_d = 0.255$, and $C_a = 0.370$. The solar distance during the DCAM3 operation was 1.35 au (astronomical unit), resulting in an SRP magnitude of $\Phi \simeq 2.5 \times 10^{-6}$ Pa. The direction vector $\hat{\mathbf{z}}$ is dependent on the orientation of DCAM3, which leads to coupling between orbital and attitude motions (Kikuchi et al., 2017). Because of the significant nutation of DCAM3, the solar angle, α , ranged between approximately 80 and 140 deg. The camera was constantly illuminated by the sun, except for the short period immediately before the collision with the asteroid surface; thus, shadowing by the asteroid is not taken into account in this research.

3.3. Attitude motion

Let $\mathbf{q} \equiv [\tilde{\mathbf{q}}^T, \dot{q}]^T$ be a quaternion vector to describe the attitude of DCAM3. The first three components, $\tilde{\mathbf{q}}$, encode information on the Euler axis, and the fourth component, $\dot{q} = \sqrt{1 - \tilde{\mathbf{q}}^T \tilde{\mathbf{q}}}$, is an auxiliary parameter defining the rotation angle about the Euler axis. This attitude representation is employed for attitude propagation, while the associated Euler angles are used to visualize the analysis results in this paper. The Euler angle set for a 1-2-3 rotation sequence is denoted by $\boldsymbol{\vartheta} = [\phi, \theta, \psi]^T$. The angles ϕ and θ represent the direction of the optical axis of DCAM3, while ψ defines its spin phase. From the definition of the camera-centered inertial frame, $\phi = \theta = 0$ corresponds to the attitude in which the optical axis is aligned with the ideal target direction. The direction cosine matrix can be expressed as a function of either \mathbf{q} or $\boldsymbol{\vartheta}$ as follows (Hughes, 2004):

$$\begin{aligned} \mathbf{D} &= (\dot{q}^2 - \tilde{\mathbf{q}}^T \tilde{\mathbf{q}}) \mathbf{E} + 2\tilde{\mathbf{q}} \tilde{\mathbf{q}}^T - 2\dot{q} [\tilde{\mathbf{q}}]_{\times} \\ &= \mathbf{R}_z(\psi) \mathbf{R}_y(\theta) \mathbf{R}_x(\phi), \end{aligned} \quad (6)$$

where \mathbf{R}_x , \mathbf{R}_y , and \mathbf{R}_z represent principal rotations about the x , y , and z axes, respectively; \mathbf{E} is an identity matrix; and $[\mathbf{a}]_{\times}$ is a skew-symmetric operator defined by the following equation for an arbitrary vector $\mathbf{a} = [a_1, a_2, a_3]^T$:

$$[\mathbf{a}]_{\times} = \begin{bmatrix} 0 & -a_3 & a_2 \\ a_3 & 0 & -a_1 \\ -a_2 & a_1 & 0 \end{bmatrix}. \quad (7)$$

The angular velocity vector of the camera-fixed frame relative to the camera-centered inertial frame is denoted by $\boldsymbol{\omega}$. A kinematic relationship exists between \mathbf{q} and $\boldsymbol{\omega}$, as described below (Wertz, 1978).

$$\dot{\mathbf{q}} = \frac{1}{2} \begin{bmatrix} -[\boldsymbol{\omega}]_{\times} & \boldsymbol{\omega} \\ -\boldsymbol{\omega}^T & 0 \end{bmatrix} \mathbf{q}. \quad (8)$$

The attitude dynamics of DCAM3 is governed by the Euler equation expressed in the camera-fixed coordinate frame as follows:

$$\mathbf{I} \dot{\boldsymbol{\omega}} = -\boldsymbol{\omega} \times \mathbf{I} \boldsymbol{\omega} + \mathbf{T}, \quad (9)$$

where \mathbf{T} is the perturbing torque and \mathbf{I} is the moment of inertia tensor. In the camera-fixed frame, the components of \mathbf{I} are given by the equation below.

$$\mathbf{I} = \begin{bmatrix} I_{xx} & I_{xy} & I_{xz} \\ I_{xy} & I_{yy} & I_{yz} \\ I_{xz} & I_{yz} & I_{zz} \end{bmatrix}. \quad (10)$$

The attitude state of DCAM3, \mathbf{q} and $\boldsymbol{\omega}$, can be obtained by numerically integrating Eqs. (8) and (9). The inertia tensor, \mathbf{I} , is estimated in the attitude determination process.

As discussed later, observations suggested that the attitude motion of DCAM3 was subject to unmodeled torque not attributable to the asteroid gravity or the SRP. Thus,

the attitude is computed based on Eq. (9) by treating the perturbing torque, \mathbf{T} , as an estimation parameter, without explicitly modeling environmental torques. Nevertheless, the magnitudes of the gravity gradient torque and SRP torque are evaluated for the discussion on attitude disturbance. The gravity-gradient torque due to the asteroid gravity is given by the equation below (Wertz, 1978).

$$\mathbf{T}_g = \frac{3GM}{r^5} \mathbf{r} \times \mathbf{I} \mathbf{r}. \quad (11)$$

In this model, we consider the contribution of only the point-mass gravity and neglect any higher-order terms. The SRP torque can be calculated using the same cylindrical model employed for SRP acceleration, as follows:

$$\mathbf{T}_p = -\Phi dhu(\mu_s C_s + \mu_d C_d + \mu_a C_a)(\mathbf{s} \times \hat{\mathbf{z}}). \quad (12)$$

This equation uses variables that are identical to those in Eq. (4). The additional parameter u represents the offset of the center of mass with respect to the center of figure along the cylinder's axis. This parameter is set to $u = -2.7\text{mm}$ according to the mechanical model of DCAM3. The derivation of the SRP torque model is also provided in the Appendix.

DCAM3 has a cylindrical shape with $I_{xx} \simeq I_{yy}$, and the external torque is small relative to the camera's angular momentum. Thus, the attitude dynamics can be approximated as torque-free motion of a spinning axisymmetric body. In this idealized situation, the angular velocity vector, $\boldsymbol{\omega}$, and the body-fixed central axis, $\hat{\mathbf{z}}$, uniformly rotate about the angular momentum vector, $\mathbf{L} \equiv \mathbf{I}\boldsymbol{\omega}$, which is inertially fixed according to the conservation of angular momentum (Wertz, 1978). These three vectors exist on the same plane, each maintaining a constant angle with respect to the others. The nutation angle is defined by the following equation as the separation angle between $\hat{\mathbf{z}}$ and \mathbf{L} :

$$\gamma = \cos^{-1} \frac{|\mathbf{L} \cdot \hat{\mathbf{z}}|}{|\mathbf{L}|}. \quad (13)$$

Let the axial and transverse moments of inertia for this axisymmetric model be $I_a \equiv I_{zz}$ and $I_t \equiv (I_{xx} + I_{yy})/2$, respectively. The angular velocity at which $\hat{\mathbf{z}}$ rotates about \mathbf{L} is called the inertial nutation rate and is given by the equation below.

$$\omega_n = \frac{|\mathbf{L}|}{I_t}. \quad (14)$$

On the other hand, the spin rate of an arbitrary body-fixed point about $\hat{\mathbf{z}}$, with respect to the orientation of \mathbf{L} , is expressed as follows (Wertz, 1978):

$$\omega_b = \left(1 - \frac{I_a}{I_t}\right)(\boldsymbol{\omega} \cdot \hat{\mathbf{z}}) \quad (15)$$

This parameter is referred to as the relative spin rate. These analytical metrics are used to characterize the numerically derived attitude profile of DCAM3 in Section 6.

3.4. Image processing

This section introduces mathematical models for the geometric processing of DCAM3 images, including those for coordinate transformation, perspective projection, the rolling shutter effect, and lens distortion. The corresponding functions are summarized in Table 5. The relationship between these mappings is illustrated in Fig. 5, which is detailed at the end of this section.

Let $[\xi, \eta, \zeta]^T$ be an arbitrary position vector expressed in the asteroid-fixed coordinate frame and $[X, Y, Z]^T$ be the corresponding position expressed in the camera-fixed coordinate frame. The transformation from the former frame to the latter frame can be expressed as follows:

$$\mathcal{S}(t, \mathbf{r}, \mathbf{q}) : \begin{bmatrix} \xi \\ \eta \\ \zeta \end{bmatrix} \mapsto \begin{bmatrix} X \\ Y \\ Z \end{bmatrix} = \mathbf{D}(\mathbf{q}) \mathbf{A}^T(t) \left(\begin{bmatrix} \xi \\ \eta \\ \zeta \end{bmatrix} - {}^{\text{AF}}\mathbf{r} \right), \quad (16)$$

where \mathbf{A} and \mathbf{D} are rotation matrices describing the transformations from the camera-centered inertial frame to the asteroid-fixed frame and to the camera-fixed frame, respectively, and ${}^{\text{AF}}\mathbf{r}$ represents the position of DCAM3 expressed in the asteroid-fixed frame. The matrix \mathbf{A} is a function of time, t , while \mathbf{D} is dependent on the camera attitude, \mathbf{q} , as given by Eq. (6). In computer vision terminology, the mapping defined by Eq. (16) corresponds to an extrinsic matrix (Bradski and Kaehler, 2008).

The subsequent projective transformation from the three-dimensional camera-fixed coordinates to the two-dimensional image coordinates expressed in pixels is given by the following equation:

$$\mathcal{P}(\mathbf{K}, \mathbf{c}) : \begin{bmatrix} X \\ Y \\ Z \end{bmatrix} \mapsto \begin{bmatrix} x \\ y \end{bmatrix} = \mathbf{K} \begin{bmatrix} X/Z \\ Y/Z \end{bmatrix} + \mathbf{c}, \quad (17)$$

where

$$\mathbf{K} = \begin{bmatrix} f_x & 0 \\ 0 & f_y \end{bmatrix}, \quad \mathbf{c} = \begin{bmatrix} c_x \\ c_y \end{bmatrix}. \quad (18)$$

The variables $[f_x, f_y]$ and $[c_x, c_y]$ represent the focal length and optical center, respectively. These parameters are fixed to values determined by on-ground experiments, which are $f_x = 1626.28\text{px}$, $f_y = 1627.62\text{px}$, $c_x = 1008.78\text{px}$, and $c_y = 1001.21\text{px}$. A three-dimensional matrix formed by \mathbf{K} and \mathbf{c} for homogeneous coordinates is called an intrinsic matrix in the field of computer vision (Bradski and Kaehler, 2008).

As the DCAM3-D imaging system employs an electronic rolling shutter, each pixel is exposed at different

Table 5

Four mappings used in image processing.

Mapping	Set	Element	Description
$\mathcal{S}(t, \mathbf{r}, \mathbf{q})$	$\mathbb{R}^3 \rightarrow \mathbb{R}^3$	$[\xi, \eta, \zeta]^T \mapsto [X, Y, Z]^T$	Coordinate transformation
$\mathcal{P}(\mathbf{K}, \mathbf{c})$	$\mathbb{R}^3 \rightarrow \mathbb{R}^2$	$[X, Y, Z]^T \mapsto [x, y]^T$	Perspective projection
$\mathcal{R}(\tau, \mathbf{q}, \omega)$	$\mathbb{R}^3 \rightarrow \mathbb{R}^3$	$[X, Y, Z]^T \mapsto [X_r, Y_r, Z_r]^T$	Rolling shutter effect
$\mathcal{L}(\mathbf{k})$	$\mathbb{R}^2 \rightarrow \mathbb{R}^2$	$[x, y]^T \mapsto [x_l, y_l]^T$	Lens distortion

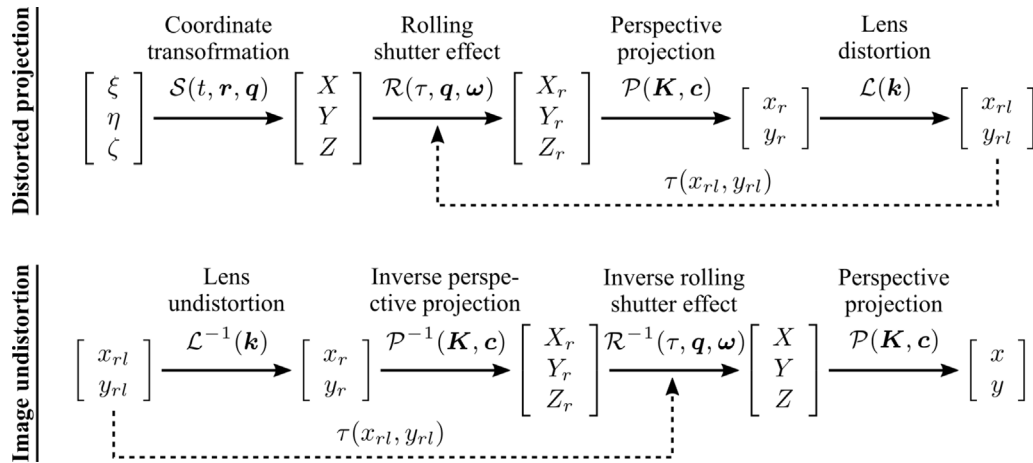


Fig. 5. Mathematical processes of distorted projection and image undistortion.

times. If the motion of a subject is fast relative to the exposure delay, the captured object is distorted on an image plane. In our case, the rapid spinning of DCAM3 caused considerable shifts in the locations of Ryugu's surface points within images. The rolling shutter effect is estimated simultaneously with the motion of DCAM3 and is corrected to produce distortion-free images. One of the classical approaches for these tasks is to model the distortion effects caused by uniform translational and rotational motions (Ait-Aider et al., 2007; Magerand et al., 2012). In this study, the translational effect is negligible because of the relatively slow orbital motion, while the rotational

effect is significant due to the fast attitude motion. Assuming uniform rotation at a constant spin rate, we validated the correction of the rolling shutter effect in on-ground experiments (Ishibashi et al., 2017). However, we found that this uniform rotation model was not sufficiently precise for actual DCAM3 images, as significant nutation induced variations in spin states, even during short exposure delays.

For these reasons, image projection and undistortion processes involve numerical integration with high temporal resolution for determining the orientation of DCAM3 at the time each pixel is exposed. The rolling shutter effect

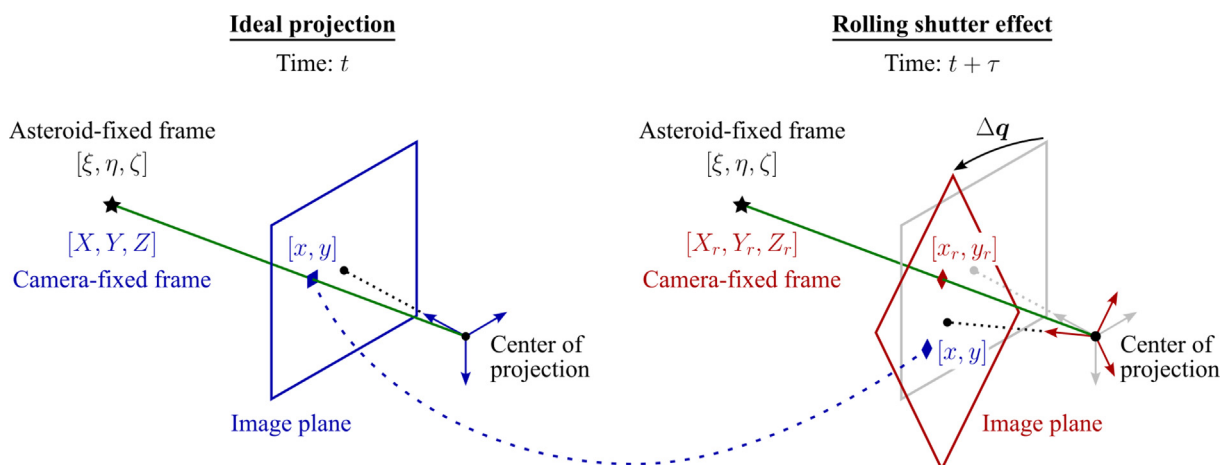


Fig. 6. Schematic illustration of the rolling shutter effect. The left part shows the ideal projection, while the right part shows the distorted projection with the rolling shutter effect.

can be expressed as the distortion where the camera-fixed position vector $[X, Y, Z]^T$ is shifted to $[X_r, Y_r, Z_r]^T$, as sketched in Fig. 6. The relationship between these two vectors is given by the equation below as a function of τ , \mathbf{q} , and ω .

$$\mathcal{R}(\tau, \mathbf{q}, \omega) : \begin{bmatrix} X \\ Y \\ Z \end{bmatrix} \mapsto \begin{bmatrix} X_r \\ Y_r \\ Z_r \end{bmatrix} = \mathbf{D}(\Delta\mathbf{q}) \begin{bmatrix} X \\ Y \\ Z \end{bmatrix}. \quad (19)$$

The quaternion $\Delta\mathbf{q}$ represents the difference in observation attitudes due to the exposure time delay and is given by the equation below.

$$\Delta\mathbf{q}(\tau, \mathbf{q}, \omega) = \begin{bmatrix} \dot{\mathbf{q}}\tilde{\mathbf{q}}_\tau - \dot{\mathbf{q}}_\tau\tilde{\mathbf{q}} - \tilde{\mathbf{q}} \times \tilde{\mathbf{q}}_\tau \\ \dot{\mathbf{q}}\dot{\mathbf{q}}_\tau + \tilde{\mathbf{q}} \cdot \tilde{\mathbf{q}}_\tau \end{bmatrix}. \quad (20)$$

The subscript ‘ τ ’ represents the attitude at time $t + \tau$, which is numerically computed from Eq. (9) for the given initial states, \mathbf{q} and ω , at time t . The time delay τ corresponding to pixel $[x, y]^T$ is obtained from the following equation:

$$\tau(x, y) = x\kappa_x + y\kappa_y, \quad (21)$$

where $\kappa_x = 2.5 \times 10^{-8}$ s/px and $\kappa_y = 6.288 \times 10^{-5}$ s/px. Because the exposure delay primarily results from vertical scanning, the value of κ_y is significantly larger than that of κ_x . The size of a DCAM3 image is 2000px \times 2000px, leading to a maximum time delay of $\tau \simeq 0.126$ s. Given that the inertial and relative spin rates of DCAM3 were 53.3 and 8.2 deg/s, respectively (see Section 6 for details), the inertial camera orientation and the camera-relative spin-axis orientation differed by approximately 6.7 and 1.0 deg, respectively, between the first and last pixels exposed. Note that Eq. (21) must be evaluated for pixel coordinates considering the effect of image distortion.

The other distortion effect considered in this research is typical lens distortion. A normalization process to transform the pixel coordinates $[x, y]^T$ into nondimensional coordinates $[\hat{x}, \hat{y}]^T$ is introduced as follows:

$$\begin{bmatrix} \hat{x} \\ \hat{y} \end{bmatrix} \equiv \mathbf{K}^{-1} \left(\begin{bmatrix} x \\ y \end{bmatrix} - \mathbf{c} \right). \quad (22)$$

Considering radial lens distortion, the distorted image point, $[x_l, y_l]^T$, can be expressed by the equation below (Heikkilä and Silvén, 1997).

$$\mathcal{L}(\mathbf{k}) : \begin{bmatrix} x \\ y \end{bmatrix} \mapsto \begin{bmatrix} x_l \\ y_l \end{bmatrix} = \begin{bmatrix} x \\ y \end{bmatrix} + \mathbf{K} \left\{ \sum_{j=1}^{n_k} k_j (\hat{x}^2 + \hat{y}^2)^j \right\} \begin{bmatrix} \hat{x} \\ \hat{y} \end{bmatrix}. \quad (23)$$

The distortion coefficients are treated as estimation parameters and are denoted by $\mathbf{k} = [k_1, \dots, k_{n_k}]$, where $n_k = 3$ in this paper.

The geometric relationship between DCAM3 and Ryugu is reconstructed by combining the four mapping functions, \mathcal{S} , \mathcal{P} , \mathcal{R} , and \mathcal{L} , which are summarized in Table 5. The analyses of DCAM3 images involve two fundamental

procedures, as shown in Fig. 5. One is the projection of an arbitrary three-dimensional point expressed in the asteroid-fixed frame onto the DCAM3 image plane, subject to both the rolling shutter effect and lens distortion. This process is required to correlate observed and computed feature points. If the pixel location with these two distortion effects is expressed as $[x_{rl}, y_{rl}]^T$, then the distorted projection is expressed as follows:

$$\mathcal{L} \circ \mathcal{P} \circ \mathcal{R} \circ \mathcal{S} : \begin{bmatrix} \xi \\ \eta \\ \zeta \end{bmatrix} \mapsto \begin{bmatrix} x_{rl} \\ y_{rl} \end{bmatrix}. \quad (24)$$

As visualized in Fig. 5, the rolling shutter effect is dependent on the exposure delay τ , which is a function of $[x_{rl}, y_{rl}]^T$. While this problem can be rigorously solved through numerical iteration (Ait-Aider et al., 2007), a different approach is adopted in the present study for brevity. We calculate approximate values for τ from the pixel coordinates of observed feature points, which typically differ by only a few pixels from the reprojected ones. The other procedure is geometric calibration, aimed at removing the rolling shutter effect and lens distortion. The composite mapping for image undistortion is given by the following equation, as depicted in the bottom part of Fig. 5:

$$\mathcal{P} \circ \mathcal{R}^{-1} \circ \mathcal{P}^{-1} \circ \mathcal{L}^{-1} : \begin{bmatrix} x_{rl} \\ y_{rl} \end{bmatrix} \mapsto \begin{bmatrix} x \\ y \end{bmatrix} \quad (25)$$

Although the inverse perspective projection, \mathcal{P}^{-1} , is a multivalued function, the degeneracy is resolved in the subsequent perspective projection, \mathcal{P} . The independent parameters presented in Table 5 and Fig. 5 are categorized as follows: \mathbf{K} , \mathbf{c} , and \mathbf{k} are common constants for all images; t , \mathbf{r} , \mathbf{q} , and ω are variables for each image; and τ is a variable for each pixel.

3.5. Least-squares estimation

3.5.1. Mathematical model

The core of simultaneous image calibration and orbit-attitude determination lies in least-squares estimation. Let $\mathbf{x} \in \mathbb{R}^{n_p}$ be a set of estimation parameters, such as state vectors, distortion coefficients, and system parameters, and let $\mathbf{z} \in \mathbb{R}^{n_o}$ be a set of observations used to determine \mathbf{x} . If the prediction function to obtain computed observables is denoted by \mathbf{h} , the associated residual vector is defined as follows:

$$\boldsymbol{\varepsilon} = \mathbf{z} - \mathbf{h}(\mathbf{x}). \quad (26)$$

The residual sum of squares to be minimized is given by the equation below.

$$J = \boldsymbol{\varepsilon}^T \mathbf{W} \boldsymbol{\varepsilon}, \quad (27)$$

where \mathbf{W} is a weighting matrix. The best estimate of \mathbf{x} satisfies $\partial J / \partial \mathbf{x} = \mathbf{0}$. This condition can be approximately reduced to the following normal equation by linearizing

about the initial estimate \mathbf{x}_* (Montenbruck and Gill, 2000; Seber and Wild, 2003):

$$\Delta \mathbf{x} = (\mathbf{H}^T \mathbf{W} \mathbf{H})^{-1} \mathbf{H}^T \mathbf{W} (\mathbf{z} - \mathbf{h}(\mathbf{x}_*)), \quad (28)$$

where $\mathbf{H} = \partial \mathbf{h} / \partial \mathbf{x}$ denotes the partial derivatives of the modeled observations with respect to the estimation parameters. The initial estimate is iteratively adjusted by an increment of $\Delta \mathbf{x}$ until this shift becomes sufficiently small. No a priori information is used for our least-squares estimations. The weighting matrix is set to $\mathbf{W} = \mathbf{Q}^{-1}$, where \mathbf{Q} is the measurement covariance defined by the equation below.

$$\mathbf{Q} = \begin{bmatrix} \varsigma_1^2 & & \\ & \ddots & \\ & & \varsigma_{n_o}^2 \end{bmatrix}. \quad (29)$$

Here, ς_i^2 denotes the variance of the i -th measurement. The measurement covariance is given as a diagonal matrix. The covariance matrix of the estimated parameters \mathbf{x} is then calculated as follows (Montenbruck and Gill, 2000):

$$\mathbf{V} = (\mathbf{H}^T \mathbf{Q}^{-1} \mathbf{H})^{-1} \quad (30)$$

While Eq. (30) provides the general form of the covariance of the least-squares solution, this paragraph introduces two distinct variations derived for specific cases. In the case of uniform measurement errors, the measurement covariance is expressed as $\mathbf{Q} = \varsigma^2 \mathbf{E}$, where \mathbf{E} is an identity matrix. Consequently, Eq. (30) is rewritten as follows:

$$\mathbf{V} = \varsigma^2 (\mathbf{H}^T \mathbf{H})^{-1}. \quad (31)$$

The equally weighted model is adopted for parameter estimations that rely on the same type of observables with unknown noise variances, such as the pixel locations of multiple feature points. In this case, the variance of the observables, ς^2 , can be approximated from the equation below. (Seber and Wild, 2003; Nelles, 2001)

$$\varsigma^2 = \frac{\mathbf{e}^T \mathbf{e}}{n_o - n_p}, \quad (32)$$

By substituting Eq. (32) into Eq. (31), we can also calculate the standard errors of the estimation parameters. The other variation involves what is known as consider covariance analysis. In some of our least-squares estimations, certain parameters are treated as consider parameters. While their uncertainties are accounted for, their a priori values remain uncorrected. Let \mathbf{b} be a vector of consider parameters and \mathbf{V}_b be its covariance matrix. The consider covariance matrix for estimated parameters, which incorporates the effect of systematic errors in the consider parameters, is given by the following equation (Tapley et al., 2004; Montenbruck and Gill, 2000):

$$\tilde{\mathbf{V}} = \mathbf{V} + \mathbf{S} \mathbf{V}_b \mathbf{S}^T. \quad (33)$$

The sensitivity matrix \mathbf{S} in this equation is computed as follows:

$$\mathbf{S} = \mathbf{V} \mathbf{H}^T \mathbf{Q}^{-1} \mathbf{H}_b, \quad (34)$$

where $\mathbf{H}_b = \partial \mathbf{h} / \partial \mathbf{b}$. In the consider covariance analysis, the consider covariance $\tilde{\mathbf{V}}$ from Eq. (33) is used in place of the noise-only covariance \mathbf{V} from Eq. (30) to evaluate the accuracy of the estimated parameters.

3.5.2. Analysis process

A step-by-step approach is adopted to solve the large-scale problem in this research. The analysis consists of six distinct steps, each of which is categorized into either the short-term estimation, long-term estimation, or final refinement introduced in Section 2.5. In each of the six steps, single or multiple least-squares estimations are conducted. These estimations are generalized as problems that aim to minimize J , which is defined in Eq. (27). The mathematical setup of these analyses is summarized in Table 6 and detailed in the subsequent paragraphs.

- Step 1: Short-term estimations based on three consecutive images are performed. The position, attitude, angular velocity, and distortion coefficient of DCAM3 (\mathbf{r} , \mathbf{q} , $\boldsymbol{\omega}$, and \mathbf{k}) are estimated from the pixel coordinates of feature points, \mathbf{p} . This process employs only 150 images (i.e., 50 sets of images) obtained up to 40 min after separation. This restriction is applied to guarantee the estimation accuracy of the lens distortion coefficients. In each estimation, the state vectors of DCAM3 at the time corresponding to the first of three images are estimated. The camera's position is assumed to be fixed during a period of ~ 2 s, while the attitude is numerically propagated within each short span to compute the rolling shutter effect. The prediction function, \mathbf{h} , in this step corresponds to the distorted image projection given by Eq. (24). The measurement covariance, \mathbf{Q} , is given as a scalar matrix; thus, all feature points are equally weighted. The standard errors of the estimated parameters are calculated from Eqs. (31) and (32).
- Step 2: A long-term estimation is performed to determine the lens distortion coefficients, \mathbf{k} . The optimal set of three distortion coefficients is calculated from the 50 sets of distortion coefficients estimated in Step 1. The solutions are simply weighted averages based on the covariance matrices derived in the previous short-term estimations. By determining the distortion coefficients first, reliable estimates of the state parameters can be obtained in subsequent steps even from images with poor viewing conditions.
- Step 3: This process involves short-term estimations similar to those in Step 1. The state parameters of DCAM3, that is, \mathbf{r} , \mathbf{q} , and $\boldsymbol{\omega}$, are treated as estimation parameters, whereas the lens distortion coefficients are fixed to the

Table 6

Mathematical setup of the least-squares estimations performed in this study. The subscripts of parameters are defined as follows: subscript ‘0’ represents the initial epoch, subscript ‘ i ’ is the index of an epoch, and subscript ‘ j ’ is the index of a feature point.

Step	Analysis type	Total number		x	z	h	Q
		Images	Calculations				
1	Short-term estimation	150	50	r_i, q_i, ω_i, k_i	$p_{i,j}$	Image projection	Scalar
2	Long-term estimation	150	1	k	k_i	Identity mapping	Diagonal
3	Short-term estimation	212	79	r_i, q_i, ω_i	$p_{i,j}$	Image projection	Scalar
4	Long-term estimation	212	1	q_0, ω_0, I, T	q_i, ω_i	Attitude propagation	Diagonal
5	Long-term estimation	212	1	r_0, \dot{r}_0, GM	r_i	Orbit propagation	Diagonal
6	Final refinement	245	245	q_i	$p_{i,j}$	Image projection	Scalar

values obtained in Step 2. The least-squares estimations rely on an expanded dataset of 212 images, which consists of 79 sets of two or three consecutive images. This dataset covers a longer period than in Step 1.

- Step 4: The attitude motion of DCAM3 is reconstructed from the discrete estimates of q and ω obtained in Step 3. The goal is to determine the orientation and angular velocity at the initial epoch. The attitude state at an arbitrary epoch can be propagated based on the kinematic and dynamic models (Eqs. (8) and (9)), which serve as the prediction function, h . In this batch estimation, the moment of inertia tensor, I , and the time-varying external torque, T , are simultaneously estimated. The parameterization of the unknown torque is outlined later in Section 6.3. The weighting matrix, $W = Q^{-1}$, is defined from the diagonal components of V computed in the previous step. The obtained continuous attitude history is used to compensate for the rolling shutter effect.
- Step 5: The trajectory of DCAM3 is determined from the series of instantaneous position estimates. This process is analogous to Step 4 for attitude dynamics. In the same manner as in Step 4, the initial position and velocity, r and \dot{r} , are estimated using the orbital model defined in Eq. (1). The SRP acceleration, a_p , is computed from Eqs. (4) and (5) with fixed model parameters. The normal vector \hat{z} is dictated by the attitude profile reconstructed in Step 4, which leads to orbit-attitude coupling. The gravitational acceleration, a_g , is given by Eqs. (2) and (3), where C_{jk} and S_{jk} are fixed to the values derived from the shape model. The asteroid’s gravitational parameter, GM , is treated either as an estimation parameter or as a consider parameter. In the former case, the gravitational parameter is estimated along with the initial state of DCAM3. In the latter case, the value of this parameter is retained as determined by previous research. The choice between these two conditions is elaborated in Section 5.4.
- Step 6: The attitude of DCAM3 at each observation epoch is refined as a final step. This process focuses on the instantaneous orientation, q , without considering any dynamics. Unlike Steps 1 and 3, which require consecutive sets of images, each least-squares estimation is based only on feature points extracted from a single image. Therefore, the final attitude refinement utilizes

a complete dataset of 245 images. The trajectory reconstructed in Step 5 is used to fix the instantaneous camera position, while the dynamic attitude data from Step 4 are interpolated to determine the rolling shutter effect for each image.

In summary, the long-term attitude and orbital motions of DCAM3 are reconstructed in Steps 4 and 5, respectively. The former is used to model the rolling shutter effect, whereas the lens distortion effect is modeled based on the distortion coefficients obtained in Step 2. By compensating for these effects, DCAM3 images can be geometrically calibrated. Higher-fidelity discrete attitude estimates, which are available at individual imaging epochs, are derived in Step 6.

4. Image calibration

4.1. Feature matching

Simultaneous image calibration and orbit-attitude determination rely on geometric information provided by image feature matching. The analysis begins by correlating feature points that have known three-dimensional locations with those captured in DCAM3 images. This task is achieved through image feature matching using DCAM3 and ONC-T data, as depicted in Fig. 3. The ONC-T images were previously geometrically calibrated and associated with pixel-by-pixel geographic data, such as latitude and longitude (Suzuki et al., 2018; Sugita et al., 2022). Fig. 7 shows an example result of mapping the feature points observed in a DCAM3 image to those in an ONC-T image.

The registration of the pairs of feature points is conducted via a hybrid of manual and automatic extraction. Due to the significant differences in optical and observational conditions between DCAM3 and ONC-T images, fully automatic feature matching is prone to false detection. Therefore, we manually register the pairs of feature points in DCAM3 and ONC-T images, enhancing the robustness of feature extraction. On the other hand, the extensive collection of DCAM3 images leads to a total of more than 100,000 feature pairs. To avoid the necessity of manual feature matching for every individual image, matched points in certain reference DCAM3 images are

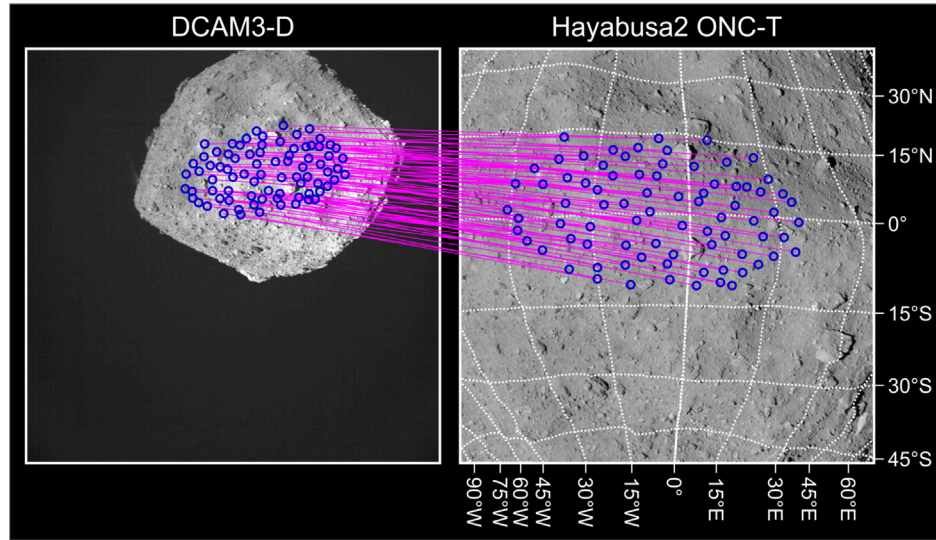


Fig. 7. Example of feature point matching between DCAM3 and Hayabusa2 images. The left panel shows the DCAM3 image obtained 1331s after separation. The right panel shows an ONC-T image obtained during the mid-altitude operation (hyb2_onc_20180801_182021_tvf_12d). Pairs of circles connected with lines represent matched feature points, whose three-dimensional locations with respect to the asteroid-fixed frame are known through the Hayabusa2 global mapping.

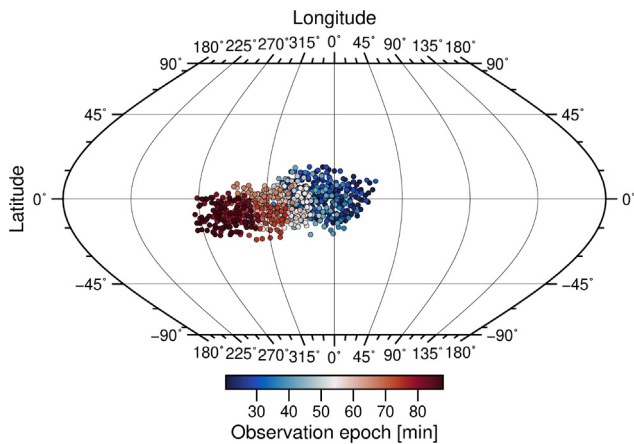


Fig. 8. Geographic locations of feature points for geometric calibration and attitude-orbit determination. The color of each dot represents the mean observation epoch (elapsed time from separation) when the corresponding feature point was observed.

algorithmically mapped to other DCAM3 images. This process is achieved by image registration using the scale-invariant feature transform (SIFT) (Lowe, 1999). Because the exact form of the mapping between two arbitrary DCAM3 images is unknown at this point, third-order bivariate polynomial transformations are applied without considering any kinematic or dynamic relationship (Brown, 1992). The polynomial coefficients are estimated from SIFT-based reference points for each image pair. To guarantee the quality of transformation, the automatic process is restricted to image pairs whose time interval is less than ~ 200 s, which corresponds to the difference in the asteroid's rotation phase of < 2.7 deg. We manually extracted feature points from 15 DCAM3 images and applied automatic extraction to the remaining 230 images.

Fig. 8 visualizes the locations of 969 unique feature points in latitude and longitude coordinates. Their three-dimensional positions with respect to the asteroid-fixed frame are derived from geographic data associated with ONC-T images. The selection of the feature points was confined to the latitude range of -30 to $+30$ deg. This is because the precise identification of feature points at higher latitudes becomes challenging owing to larger emission angles. As shown in Fig. 8, the locations of the adopted points shift to the west in later epochs in accordance with the asteroid rotation.

The number of feature points captured in each DCAM3 image is approximately 65 on average and ranges between

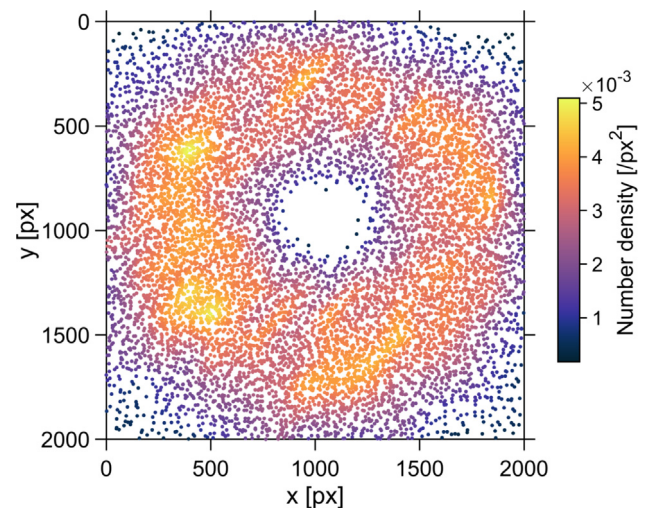


Fig. 9. Pixel locations of the observed feature points for geometric calibration. The points are projected on the DCAM3 image plane and color-coded according to their number densities.

12 and 85. The cumulative total number of observed feature points employed in the orbit and attitude determination is 13,841. Among them, 10,215 were used for lens distortion correction, whose pixel locations are shown in Fig. 9. This figure indicates that the observed feature points are distributed across the entire image plane even though the asteroid occupies only a part of the field of view of DCAM3 (see Fig. 7). The density profile shown in Fig. 9 exhibits an annular distribution. Feature points are scarcely distributed at the center because the ideal camera orientation was designed such that the optical axis is directed toward the SCI crater near the limb of the asteroid. The widespread feature distribution, which is due to the spin and rotation of DCAM3, facilitates precise geometric calibration.

4.2. Reprojection error

In short-term estimations outlined in Section 2.5, the imaging geometries are reconstructed based on the three-dimensional location data of the extracted feature points. Fig. 10 shows an example result of the short-term estimation. This figure compares the distribution of manually selected feature points with that of reprojected points computed from the corresponding geographic information and mathematical models. The right panel shows that our image processing method, which is based on the distorted projection model given by Eq. (24), replicates the locations of feature points captured within the image plane. This observation implies that the estimated distortion model is sufficiently accurate because otherwise the observed and computed feature points deviate from each other, as depicted in the left panel of Fig. 10. The precise reconstruction of the geometric relationship between DCAM3 and Ryugu contributes to high-fidelity orbit and attitude determination.

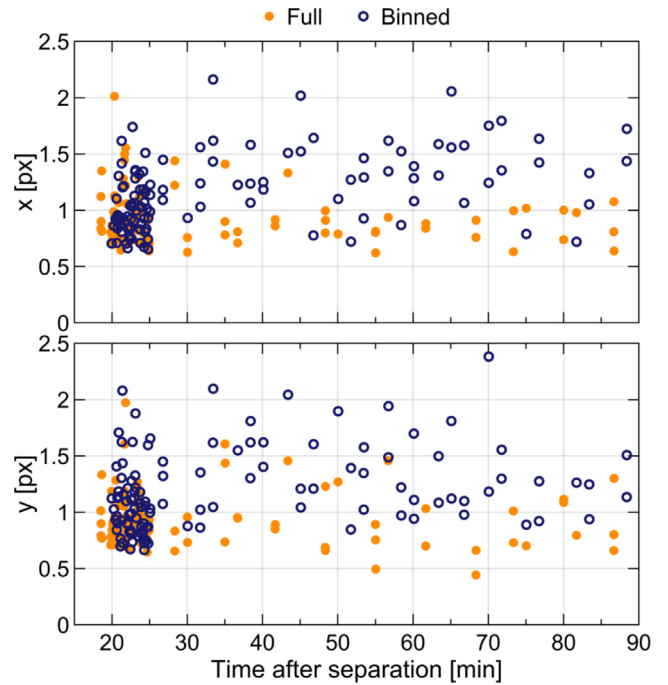


Fig. 11. Residuals of image feature matching expressed in pixels. The filled and open markers correspond to full-size images and downsized images obtained by 5×5 pixel binning, respectively. The sizes of the binned images are adjusted to match the sizes of the original images for fair comparison.

The quality of geometry reconstruction can be evaluated by reprojection errors, defined as the root-mean-square (RMS) errors between observed and computed feature points. Fig. 11 depicts the reprojection errors associated with the short-term estimations in Step 3 (see Section 3.5.2). The RMS errors of the horizontal and vertical pixel components are plotted for all 212 images. The reprojection errors typically fall between 0.5 and 1.5px for full-size images. The errors are reasonably small given that feature

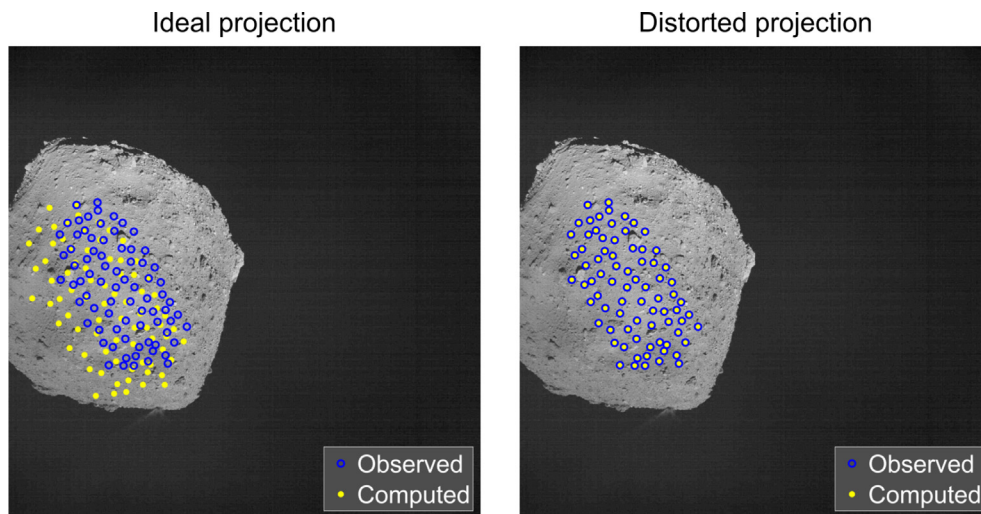


Fig. 10. Example of feature reprojection onto the DCAM3 image plane. The observed and computed feature points are represented by open and filled circles, respectively. The computed feature points are obtained by the ideal perspective projection in the left panel and by the projection accounting for the image distortion in the right panel. Both panels display the same image captured 1472s after separation.

matching between DCAM3 and ONC-T images relies on manual feature extraction. Pixel binning led to a slight increase in reprojection errors, typically by up to ~ 2 px. This is presumably because the accuracy of feature detection degrades when images have lower effective resolutions.

The uncertainty in feature point locations is not trivial and thus is estimated from the reprojection errors based on Eq. (32). The estimated variance, ζ^2 , for each set of images is then converted to the covariance matrix of the estimated parameters (i.e., the distortion coefficients and the state parameters of DCAM3) using Eq. (31). However, the assumption of unbiased and uncorrelated observables often underestimates absolute measurement uncertainties (Tapley et al., 2004). Past studies have also discussed similar issues regarding the positional uncertainties of landmarks on small bodies (McMahon et al., 2018; Ernst et al., 2023). In our case, there exist at least two possible error sources that do not necessarily appear as random reprojection errors.

One is the systematic error in reference geographic data associated with ONC-T images. As described in Section 2.3, the ground sample distances of the ONC-T images and DCAM3 images used in this research are approximately comparable. Therefore, if pixel-scale ambiguity in latitude and longitude coordinates is assumed, the locations of feature points captured in DCAM3 images can include bias errors on the order of 1 px. The other source is mismodeling of surface topography, which could induce correlations in the errors of feature point measurements. Watanabe et al. (2019) compared two independent global shape models of Ryugu, one created via SFM and the other via stereophotoclinometry, and found that the RMS difference between these models was 1.75 m in height. This height difference corresponds to ~ 1 px when viewed from 1 km away at an emission angle of 20 deg. From these observations, we apply additive corrections equivalent to 2 px to residual vectors in short-term estimations, as a rule of thumb. Consequently, the estimated parameters are deweighted when used as measurements in subsequent long-term estimations. The lack of a true model complicates the validation of measurement errors; nevertheless, the postfit residuals presented in the following sections show reasonable agreement with the expected measurement uncertainties. Although these errors can be handled in a more sophisticated manner, such as through bias estimation, we leave this topic for future research.

4.3. Distortion estimation

The distortion profile of each DCAM3 image is composed of lens distortion and the rolling shutter effect. As described in the workflow in Section 3.5.2, the former effect is determined by the lens distortion coefficients obtained in Step 3, whereas the latter effect is replicated based on the attitude motion reconstructed in Step 4.

The estimation results for the lens distortion coefficients are shown in Fig. 12. The short-term estimations, each of

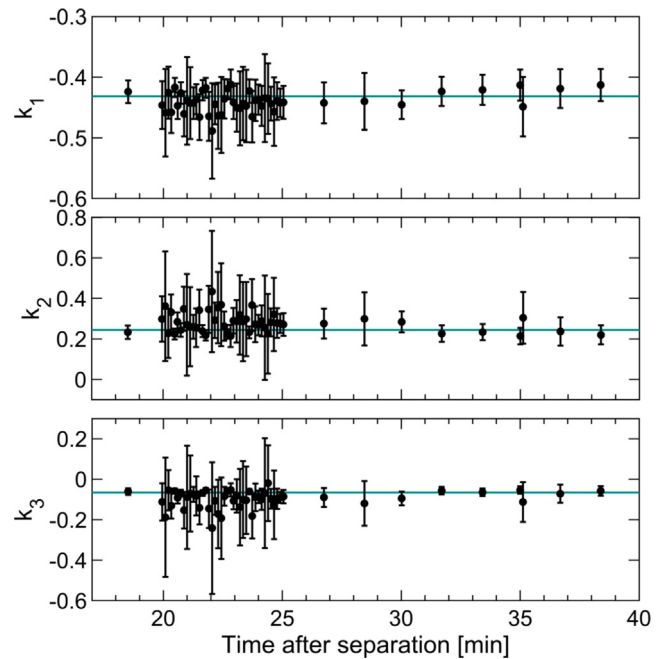


Fig. 12. Estimation of the lens distortion coefficients. The dots indicate estimated values for different observation epochs, and the associated error bars represent 2σ uncertainties. The horizontal lines show the weighted means of the distortion coefficients.

Table 7

Distortion coefficients of DCAM3 estimated from in-flight images.

Coefficient	Estimated value	Standard error
k_1	-0.4316	0.0020 (0.5%)
k_2	+0.2448	0.0039 (1.6%)
k_3	-0.0659	0.0020 (3.0%)

which was conducted based on a set of three images, yielded 50 distinct sets of estimated distortion coefficients. Considering their values and uncertainties, we calculate the optimal coefficients as weighted means. The estimated values of k_1 , k_2 , and k_3 are listed in Table 7. Fig. 12 indicates that the mean values are consistent with the short-term estimates within their uncertainty ranges in most cases. The uncertainties in the short-term estimates are dominated by the numbers and pixel locations of the observed feature points. It seems that data from low-frequency observations tend to have smaller errors compared to those from high-frequency observations. This is presumably because the asteroid tends to appear near the edge of the field of view, where pixel locations are sensitive to distortion coefficients, in the latter part of the observation period. As summarized in Table 7, the standard errors of the optimal estimates of k_1 , k_2 , and k_3 are reasonably small, measuring 0.5%, 1.6%, and 3.0%, respectively.

Fig. 13 compares the lens distortion profiles obtained through this research and the on-ground experiment (Ishibashi et al., 2017). This graph shows the relationship between the pixel distances from the optical center of a distortion-free image and those of a distorted image. The

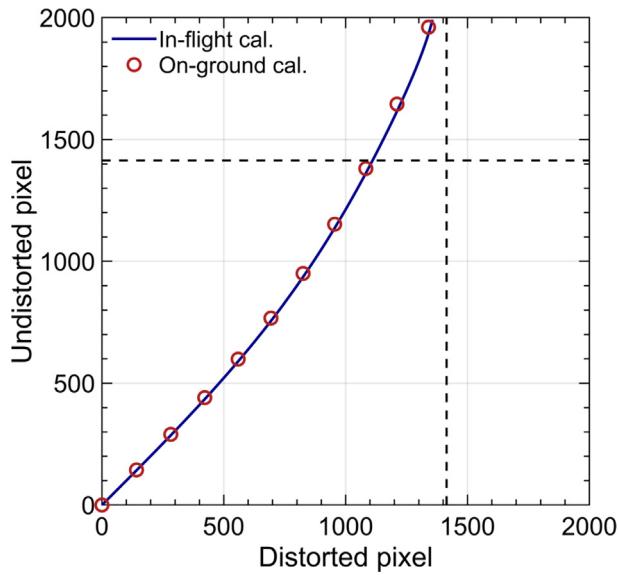


Fig. 13. Relationship between distorted and undistorted pixels from the optical center. Our in-flight calibration result is represented by the solid curve, while the prelaunch calibration result is represented by circles. The horizontal and vertical dashed lines indicate the half-diagonal distance of $1000\sqrt{2}$ px.

in-flight and on-ground calibration results show similar profiles, but the former exhibits slightly less distortion. This discrepancy is presumably due to differences in environmental conditions, such as temperature and vacuum degree. The distortion magnitudes at pixel distances of 500, 1000, and $1000\sqrt{2}$ px in an undistorted image are approximately 19, 132, and 304 px, respectively. The corresponding uncertainties in the distortion magnitudes are approximately 0.1, 1, and 4 px. This level of uncertainty satisfies the scientific requirements specified in Ishibashi et al. (2017). The caveat is that the validity of the distortion curve is guaranteed only within the region where feature points are captured. The valid region approximately corresponds to a radial distance of 1356 px for a distorted image and to 1990 px for an undistorted image. The resultant two-dimensional radial distortion field is visualized in the left panels of Fig. 14.

In contrast to static lens distortion, the rolling shutter effect varies over time because it is dependent on the dynamic attitude state of the camera. This attitude dependency is modeled in Eqs. (19) and (20). An example profile of the rolling shutter effect is provided in the middle panels of Fig. 14. In general, the rolling shutter distortion tends to increase toward the bottom of the image plane because of a

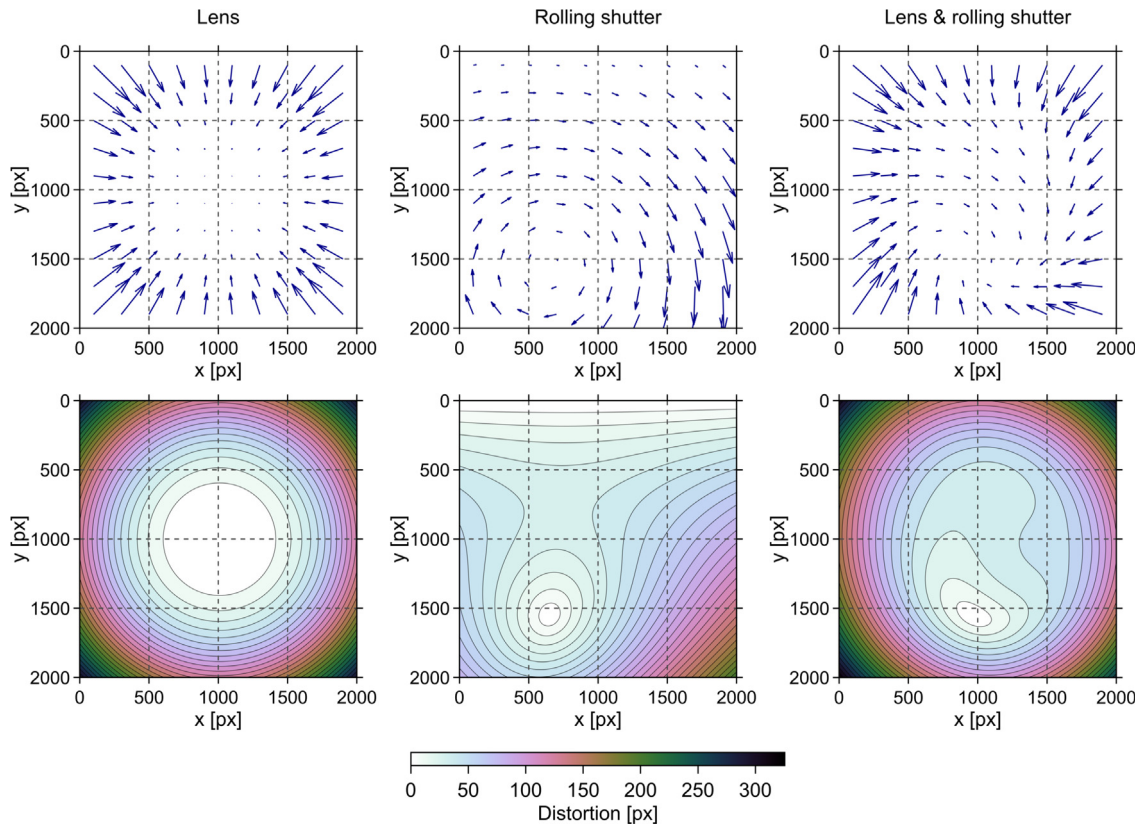


Fig. 14. Examples of distortion maps for lens distortion (left), the rolling shutter effect (center), and their combined effect (right). In the top three panels, the directions and relative magnitudes of distortions are visualized by the directions and lengths of arrows, respectively. The bottom three panels show the absolute magnitudes of distortions as contour maps. These maps are for the DCAM3 image obtained 1222 s after separation and are expressed with respect to the undistorted image plane.

longer exposure delay. In addition, there is a specific point at which the distortion becomes null. This point corresponds to the direction of the instantaneous spin axis of DCAM3. As a result, the distortion field of the rolling shutter effect features a spiral profile. The rolling shutter distortion is computed for each image according to the long-term attitude data presented in Section 6.1. To accurately capture the nonlinear characteristics of the distortion profile, the time interval for attitude propagation is set to 5 ms, which is sufficiently shorter than the 126 ms delay between the exposure of the first and last pixels.

The lens distortion and rolling shutter effect have comparable magnitudes, both leading to deviations of up to several hundred pixels. Therefore, the superposition of these two effects complicates the distortion profile, as illustrated in the right panels of Fig. 14. The maximum distortion varies depending on the image, ranging approximately from 300 to 400 px. The correction of such significant, nonuniform, time-varying distortions is a challenging task, and is the primary focus of the next section.

4.4. Distortion correction

DCAM3 images can be geometrically corrected by applying an inverse operation of the distorted projection. The calibration process, which is represented by Eq. (25), relies on the estimated distortion model. An example result is shown in Fig. 15. This figure compares the raw, corrected, and simulated DCAM3 images. The simulated image is generated based on the Hapke photometry model (Hapke, 2012), asteroid shape model, and estimated viewing conditions. The Hapke model parameters for Ryugu are provided in Tatsumi et al. (2020). The asteroid limb computed from the simulated images is plotted in each panel of Fig. 15. The left panel demonstrates that the limb profile in a raw image is significantly distorted. In contrast, the middle and right panels display almost geometrically identical images, signifying that the complex distortion has been precisely corrected.

The reconstructed geometric relationship between the camera and asteroid is used to generate geographic data

associated with each DCAM3 image. For instance, the latitude, longitude, and observation distance corresponding to each image pixel can be computed as depicted in the top two panels of Fig. 16. This information is indispensable for estimating the three-dimensional evolution of SCI impact ejecta. The other useful geometric parameters are the incidence, emission, and phase angles of an arbitrary surface point, which are defined as the angle between the surface normal and the vector pointing from the surface point to the sun, the angle between the surface normal and the vector pointing from the surface point to the camera, and the angle between the vectors pointing from the surface point to the sun and to the camera, respectively. These metrics are displayed in the bottom panels of Fig. 16 and used to generate the simulated image provided in Fig. 15. The geometric parameters can also serve as inputs for the radiometric calibration of DCAM3 images, which is one of the primary tasks of our future research.

5. Orbit determination

5.1. Reconstructed trajectory

As explained in Section 3.5.2, the long-term orbital motion of DCAM3 is reconstructed in Step 5 using the discrete position estimates obtained in Step 3. The estimated trajectory is illustrated in Fig. 17. The camera passed approximately 1 km above the SCI crater and traveled more than one round with respect to the asteroid-fixed frame. The trajectory of DCAM3 expressed in the inertial frame has a semielliptical shape with a periapsis close to the asteroid surface. This suborbital flight is retrograde with respect to the asteroid rotation. The estimation results indicate that DCAM3 primarily flew above the southern hemisphere of the asteroid and impacted near the equatorial ridge.

Fig. 18 shows the altitude histories relative to the asteroid surface, the asteroid center, and the SCI crater. The flight time until the camera impacted the asteroid surface was approximately 380 min. Because the last valid image was obtained 207 min after separation, all the images were

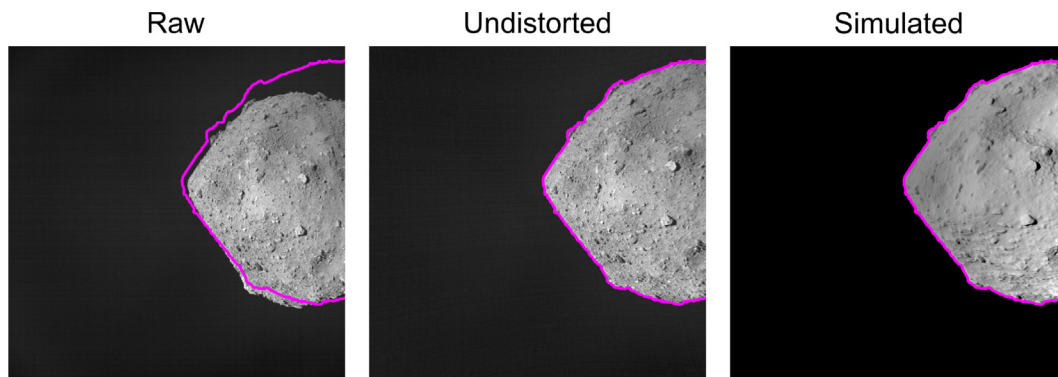


Fig. 15. Comparison between the raw, undistorted, and simulated images. The solid curve in each panel depicts the ideal asteroid limb computed from ray tracing. These images correspond to the same observation epoch, 1222 s after separation.

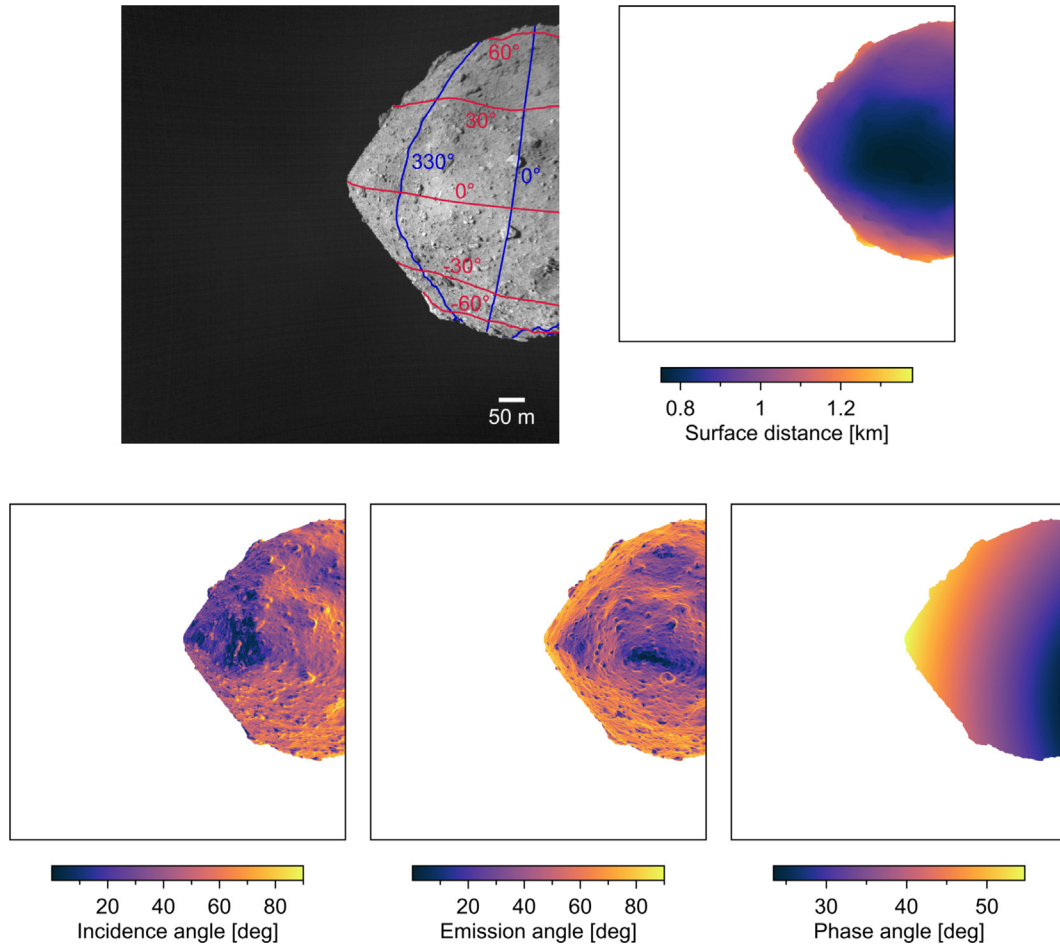


Fig. 16. Examples of geometry maps derived from simultaneous geometric calibration and attitude-orbit estimation. In the top left panel, latitude and longitude lines are overlaid on the undistorted image shown in Fig. 15. The scale bar in this panel represents the horizontal distance evaluated at the intersection between the equator and prime meridian. The top right panel is the contour map of observation distances. The bottom three panels display the distributions of incidence, emission, and phase angles.

presumed to be captured prior to the collision. The radial distance from the center of Ryugu was 1.2 km at the separation point and reached a maximum of 1.4 km at ~ 120 min after separation. The distance between DCAM3 and the asteroid surface did not exceed 1 km. The SCI detonated 21.8 min after DCAM3 separation, and a distinct ejecta curtain was visible for ~ 500 s (Arakawa et al., 2020; Wada et al., 2021). Within this period, the distance between DCAM3 and the SCI impact point ranged between 1.0 and 1.1 km. Given that the pixel scale of DCAM3 is ~ 0.615 mrad/px (Ogawa et al., 2017; Ishibashi et al., 2017), the camera observed the SCI impact point with spatial resolutions of 0.6–0.7 m/px.

The time histories of the state variables expressed in the asteroid-fixed frame are plotted in Fig. 19. The orbit determination relies on DCAM3 images acquired within 90 min after separation; hence, the trajectory beyond that time frame is extrapolated based on the dynamical model. As shown in the top left panel in Fig. 19, the instantaneous estimates fit the overall profile well. Because of its retrograde motion, the camera's velocity with respect to the

asteroid-fixed frame was faster than the tangential velocity caused by the asteroid spin, as indicated in the bottom left panel. Within the time range of images used, the orbital velocity of DCAM3 relative to the asteroid-fixed frame was 38–40 cm/s, whereas that relative to the asteroid-centered inertial frame was 10–13 cm/s.

The residual profiles associated with the batch estimation are provided in the top right panel of Fig. 19. The discrete position estimates are consistent with the best fit trajectory within their error ranges for most of the data points. Fig. 19 also demonstrates that the observation uncertainty increases over time. This is because the asteroid gradually moved out of the camera's field of view, as depicted in Fig. 4, and the number of observed feature points decreased. The fitting residuals (RMS errors) along the x_{AF} , y_{AF} , and z_{AF} coordinates are 4.0, 5.1, and 6.2 m, respectively, as summarized in Table 8. This table also lists the uncertainties in the initial position and velocity at the separation point, which are obtained via the batch least-squares estimation. These uncertainties are relatively small, with standard errors less than 0.8 m and 0.5 mm/s for each

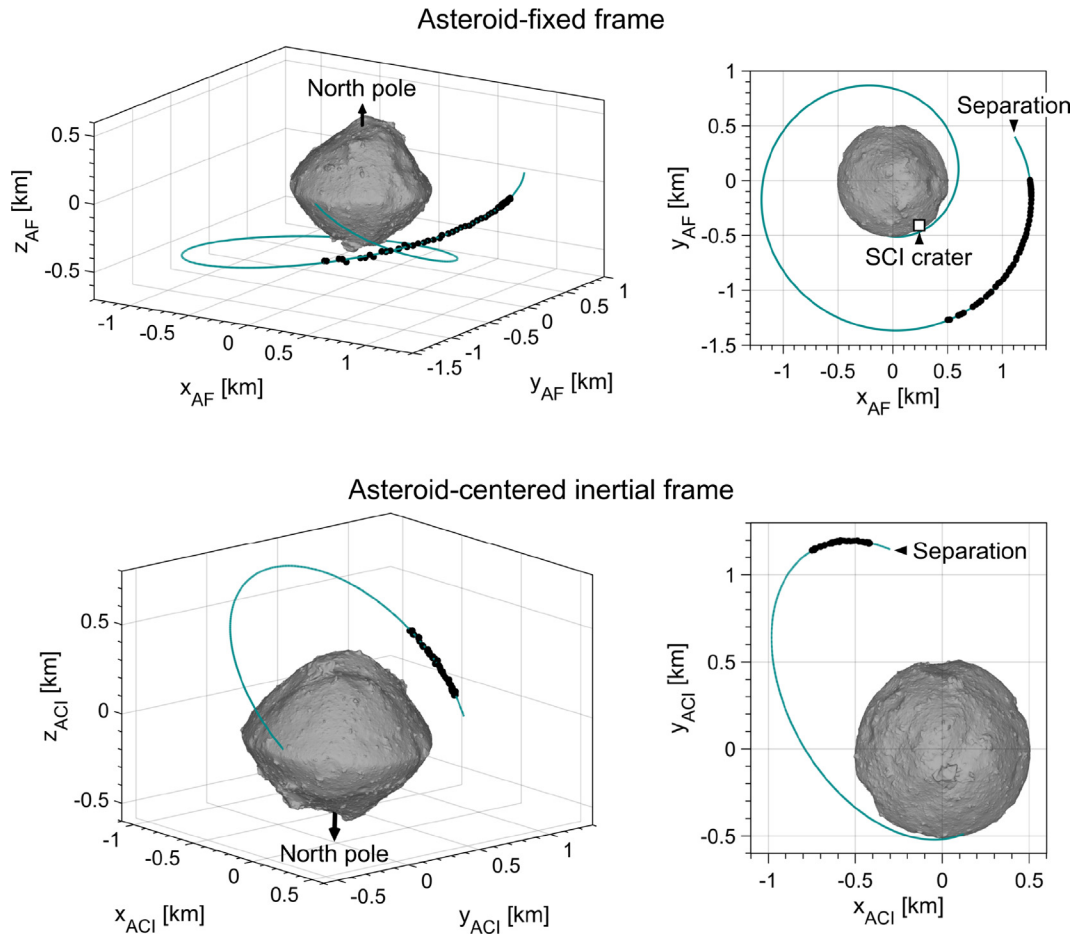


Fig. 17. Estimated orbital motion of DCAM3 expressed in the asteroid-fixed coordinate frame (top) and the asteroid-centered inertial coordinate frame (bottom). In each panel, the dots represent the instantaneous estimates of the position of DCAM3, and the solid curve depicts the reconstructed continuous profile. The location of the SCI crater is represented by the square marker in the top right panel. Because the asteroid rotates with respect to the inertial frame, the bottom panel shows the asteroid's orientation at the moment of the DCAM3 collision.

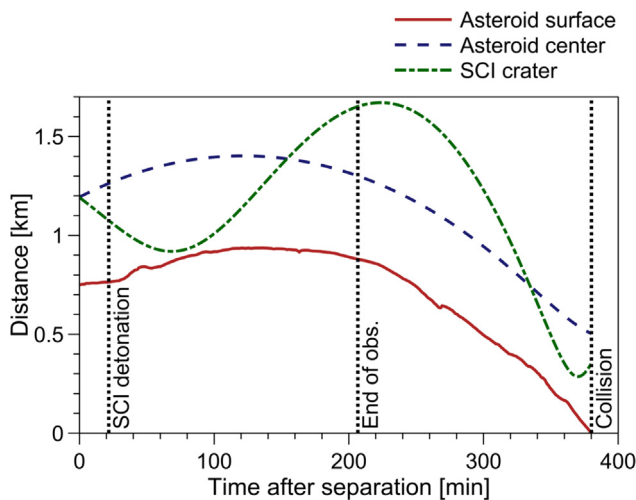


Fig. 18. Reconstructed altitude history of DCAM3. The solid, dashed, and dot-dashed curves depict the distance from the asteroid surface in the radial direction, the distance from the center of mass of the asteroid, and the distance from the SCI impact point, respectively. The epochs indicated by the vertical dotted lines correspond to the SCI detonation, the end of the DCAM3 observation sequence, and the collision of DCAM3 with the asteroid.

axis of the asteroid-fixed frame. The scale of the positional uncertainty is approximately equivalent to the spatial resolution of DCAM3 evaluated at the SCI impact point.

Fig. 20 depicts the time histories of three different accelerations acting on DCAM3. The point-mass gravity and second-order zonal gravity are computed from the reconstructed trajectory. The SRP acceleration is attitude-dependent and thus exhibits high-frequency variations in the actual dynamics. To reduce the computational cost, this effect is averaged over one nutation period for the mean nutation profile, which is discussed in Section 6.1. Fig. 20 indicates that the magnitude of the SRP acceleration is $\sim 2 \times 10^{-8} \text{ m/s}^2$, which is at least three orders of magnitude smaller than the gravitational acceleration. At the DCAM3 separation altitude, the magnitude of the second-order zonal gravity is approximately 1% of that of the point-mass gravity.

5.2. Surface impact

Fig. 21 visualizes the footprint of the reconstructed trajectory expressed in the latitude-longitude coordinate

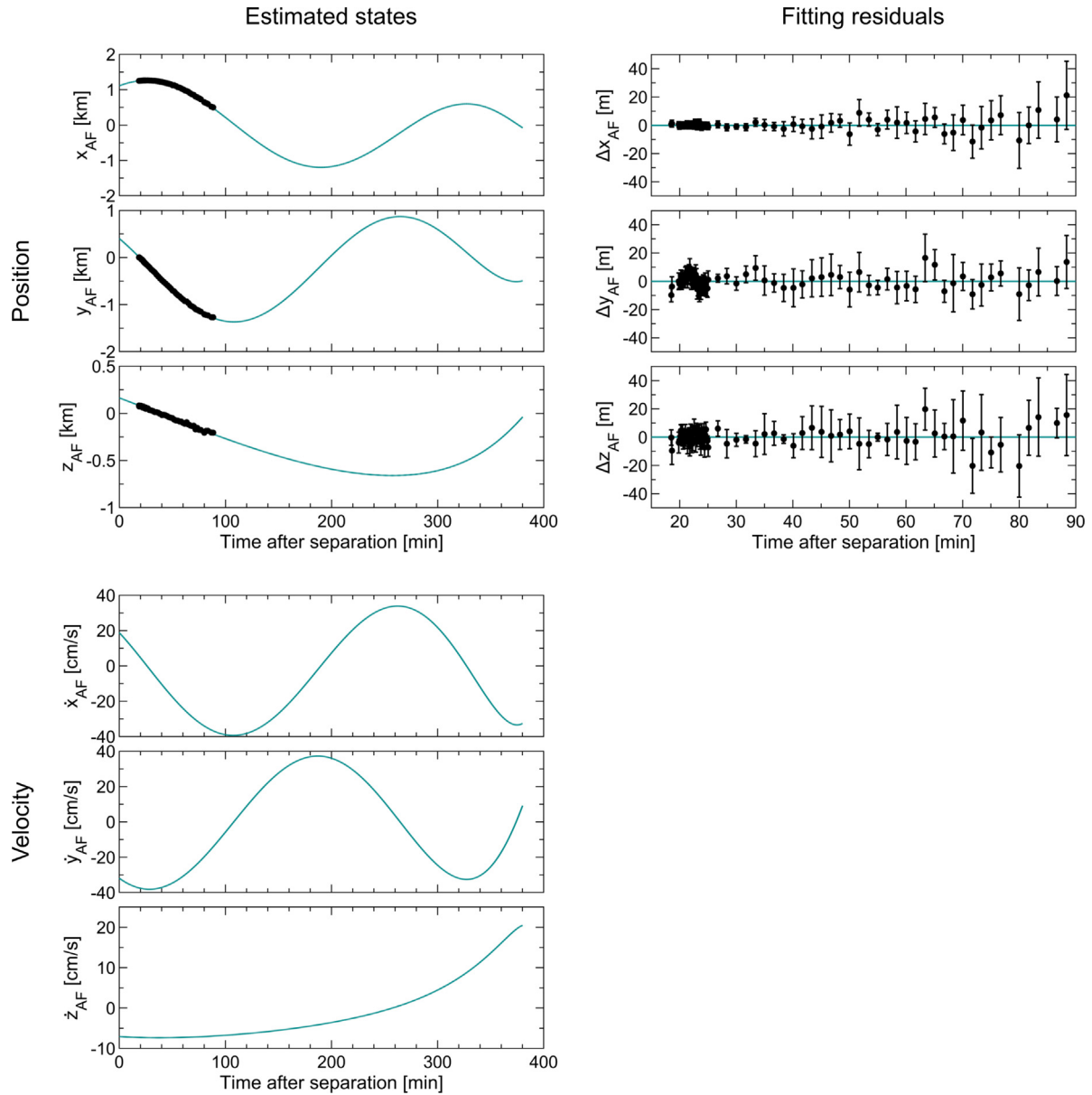


Fig. 19. Temporal variations in the estimated orbital states of DCAM3 with respect to the asteroid-fixed frame. The estimated positions (top left), the estimated velocities (bottom left), and the fitting residuals for the positions (top right). The dots show instantaneous estimates. The curves in the state plots depict the fitted profiles, while the error bars in the residual plots indicate 2σ uncertainties. The time scales of the state plots and residual plots are different.

Table 8

Fitting residuals and estimation uncertainties for the position and velocity components.

Parameter	Variable	RMS error	Uncertainty
Position	x_{AF}	4.03 m	0.56 m
	y_{AF}	5.05 m	0.78 m
	z_{AF}	6.23 m	0.79 m
Velocity	\dot{x}_{AF}	—	0.45 mm/s
	\dot{y}_{AF}	—	0.41 mm/s
	\dot{z}_{AF}	—	0.44 mm/s

frame. The trajectory footprint is situated below the equator except for immediately after separation. This figure also shows the dispersion of possible impact points computed

via Monte Carlo analysis incorporating the uncertainties in the initial state of DCAM3 and the gravitational parameter of Ryugu. The number of trials in the Monte Carlo simulation is 100,000. Considering the 2σ level of error, the estimated time when DCAM3 reached the asteroid surface ranges between 08:27 and 08:44 on April 5, 2019. Consequently, the flight time is estimated to be $380.1^{+9.2}_{-7.4}$ min.

The landing ellipse is approximately defined by the two-dimensional Gaussian distribution in the equirectangular projection. The latitude and longitude of the impact point for the best-fit trajectory are -4.4 and 261.0 deg, respectively. The uncertainty ellipse is elongated in the longitudinal direction because of the asteroid rotation and the error in impact timing. The uncertainty in the impact location is

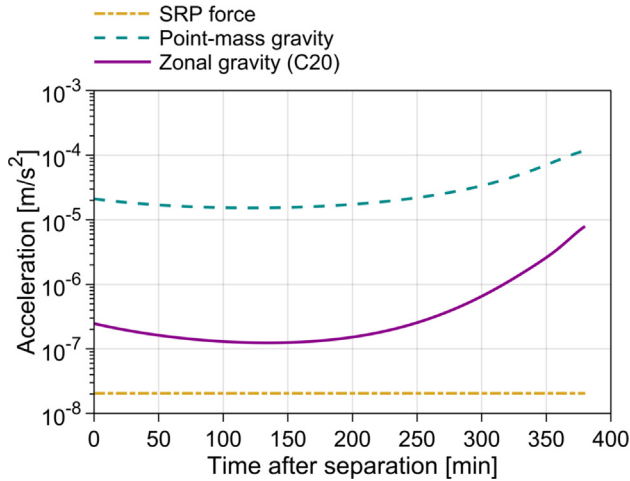


Fig. 20. Comparison of the external forces acting on DCAM3. The dot-dashed, dashed, and solid curves show the time histories of the SRP force, point-mass gravity, and second-order zonal gravity, respectively, from separation to impact.

~ 4 deg in latitude and ~ 17 deg in longitude. Although the estimated impact region is partially covered in the pre- and post-cratering surveys conducted by Hayabusa2, no clear traces of impact or landing of DCAM3 have been found. This is reasonable considering the limited optical resolution of ~ 18 cm/px, which is larger than the size of DCAM3 itself.

The estimated impact velocity relative to the asteroid surface is 39.5 cm/s. By decomposing the velocity vector into normal and tangential directions at the impact point, the normal and tangential impact velocities are determined to be 13.9 and 37.0 cm/s, respectively. According to this estimation, the impact angle, defined as the angle between the DCAM3 trajectory and the local horizontal, is as small as approximately 21 deg, which could lead to ricocheting from the asteroid surface (Çelik et al., 2019).

5.3. Separation performance

With the orbit estimation results, the performance of the DCAM3 separation in the actual space environment can be evaluated. Because employing a deployable camera for small-body exploration is a novel concept, the performance assessment establishes a benchmark for future missions. In addition, the comparison between preflight predictions and in-flight performance serves as supporting evidence for the reconstructed trajectory.

Fig. 22 illustrates the locations of DCAM3 at the epochs of DCAM3 separation and SCI impact, which are expressed in the asteroid-centered inertial frame. This figure indicates that the predicted dispersions envelope the actual DCAM3 positions. The reconstructed locations fell between the 1σ and 2σ errors at both epochs, which contributed to successful monitoring of the SCI impact event. The DCAM3 separation accuracy is directly tied to the performance of the Hayabusa2 guidance involving a complicated sequence of feed-forward maneuvers. The x_{ACI} , y_{ACI} , and z_{ACI} components of the positional deviation at the separation point are -10.7, 24.3, and -10.8 m, respectively, and the norm is 28.7 m. Note that the reconstructed position is subject to an uncertainty on the order of 1 m, as discussed in Section 5.1.

By combining the DCAM3 state information and Hayabusa2 tracking data, we calculate the separation velocity, that is, the velocity of DCAM3 with respect to Hayabusa2 at the moment of detachment. The time history of the range rate of Hayabusa2 obtained through on-ground Doppler measurements is plotted as dots in Fig. 23. The reaction force upon separation causes a slight shift in the spacecraft velocity on the order of 1 mm/s. Based on the range rate data, we estimate the Hayabusa2 velocity and thereby the DCAM3 separation velocity.

The SCI operation was designed such that DCAM3 was ideally detached in the earthward direction, which is sensi-

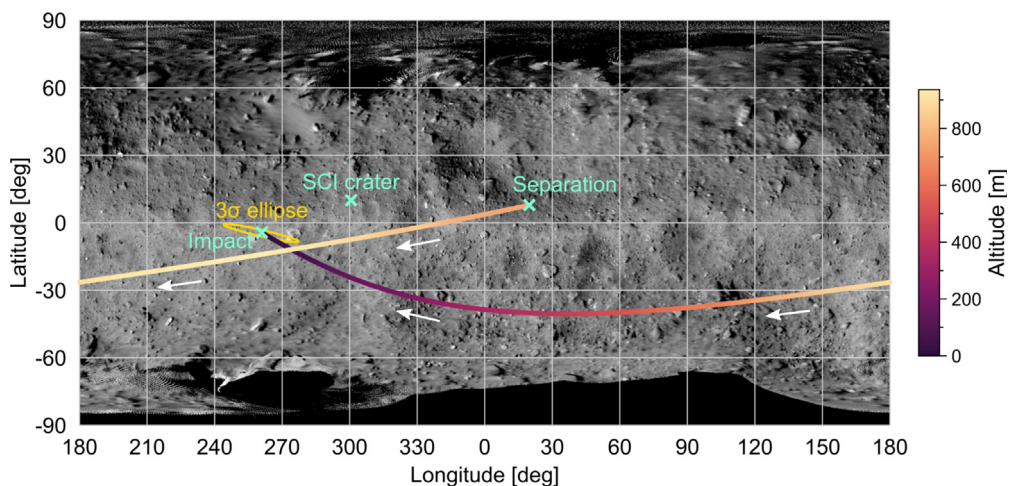


Fig. 21. Reconstructed trajectory footprint of DCAM3 displayed on the global mosaic image of Ryugu. The footprint is color-coded based on surface altitudes. The ellipse centered at the predicted impact point represents the 3σ uncertainty approximated by the two-dimensional Gaussian distribution in the latitude and longitude coordinates.

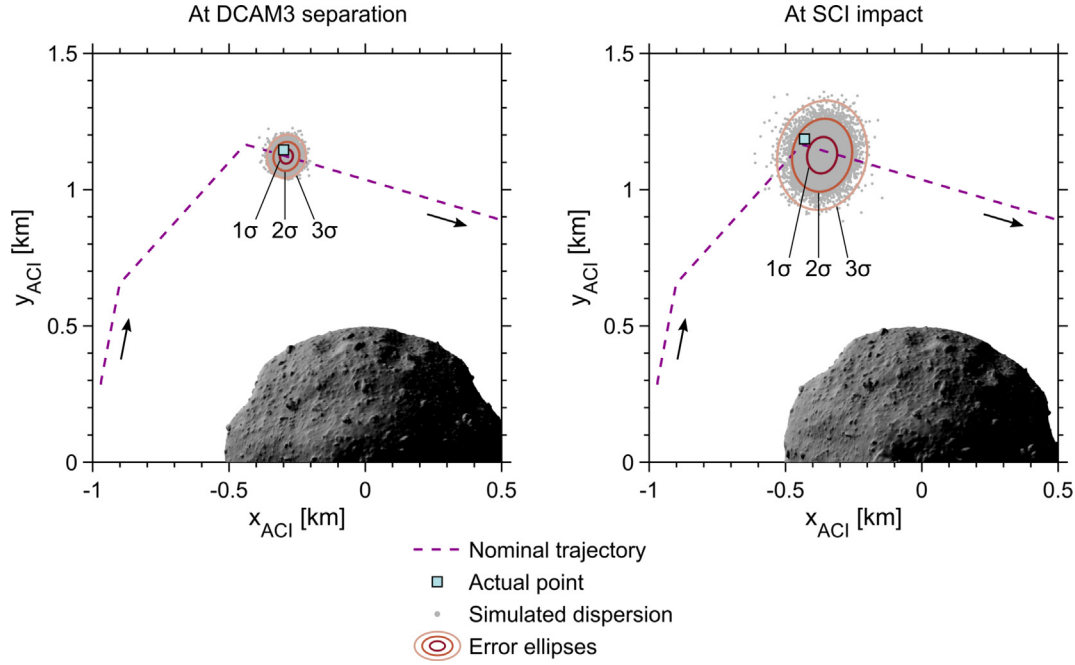


Fig. 22. Predicted and actual DCAM3 positions at the time of DCAM3 separation (left) and the time of SCI impact (right). The positions are expressed in the asteroid-centered inertial frame. In each panel, the dashed line depicts the nominal Hayabusa2 trajectory for the SCI operation, and the square marker indicates the actual DCAM3 position estimated in this research. The dispersion of the DCAM3 locations predicted by a Monte Carlo analysis is represented by dots along with the associated error ellipses. The orientation of Ryugu with respect to the inertial frame is also shown for each epoch..

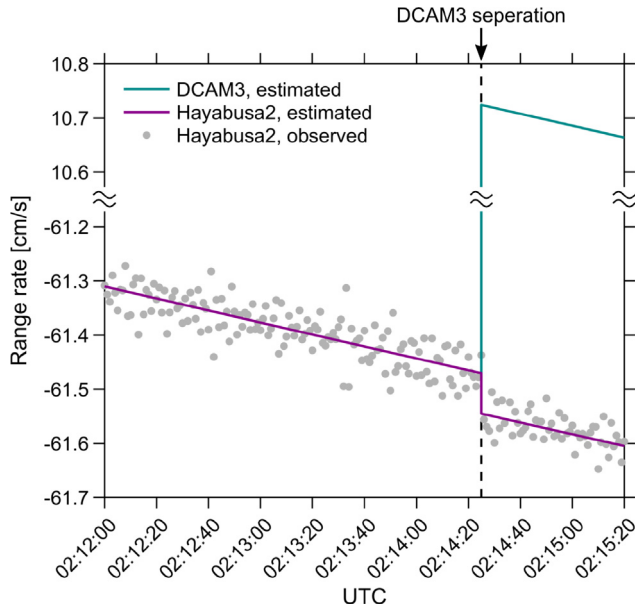


Fig. 23. Estimated line-of-sight range rates of DCAM3 and Hayabusa2. The green and purple lines depict the estimated velocities of DCAM3 and Hayabusa2, respectively. The dots represent the range rates of Hayabusa2 observed at a ground station. A range rate with a positive value signifies that an object is moving toward Earth.

tive to Doppler measurements. Therefore, the earthward component of the Hayabusa2 velocity immediately before separation is treated as an estimation parameter. The other velocity components at the same epoch are fixed at approximate values obtained from the integration of Hayabusa2 accelerometer data. The position of Hayabusa2 at the

moment of detachment is assumed to be identical to that of DCAM3 estimated in this work. The spacecraft velocities before and after separation are related by the following momentum conservation law:

$$(m_{SC} + m)v_{SC}^- = m_{SC}v_{SC}^+ + mv^+, \quad (35)$$

where m_{SC} and m are the masses of Hayabusa2 and DCAM3, respectively, v_{SC}^- and v_{SC}^+ are the velocities of Hayabusa2 immediately before and after separation, respectively, and v^+ is the given velocity of DCAM3 immediately after separation. Note that the mass of Hayabusa2, m_{SC} , does not include the mass of DCAM3, even prior to separation. Then, the range rate of Hayabusa2 at an arbitrary epoch can be computed by integrating either forward or backward from the separation point. Note that the orbital motion of the spacecraft is modeled as a two-body problem incorporating higher-order gravitational effects. The separation velocity, Δv , and the separation direction angle, χ , are defined as follows:

$$\Delta v = v^+ - v_{SC}^+, \quad (36)$$

and

$$\chi = \cos^{-1} \left(\frac{\Delta v \cdot e}{|\Delta v|} \right), \quad (37)$$

where e is a unit vector pointing from the spacecraft to Earth.

Fig. 23 shows the optimal velocity profile that best fits the observed range rate. The spacecraft velocities both before and after DCAM3 detachment agree with the Dop-

pler measurements. From the reconstructed velocities of Hayabusa2 and DCAM3, the separation velocity is determined to be $|\Delta \mathbf{v}| = 72.7 \text{ cm/s}$. This value is consistent with the designed performance of $70 \pm 7 \text{ cm/s}$ (Sawada et al., 2017). The resultant shift in the spacecraft velocity was 0.75 mm/s . The separation direction was $\chi = 6.5 \text{ deg}$, which was less than the predicted maximum value of 10 deg (Sawada et al., 2017). The corresponding lateral velocity disturbance was $\sim 8 \text{ cm/s}$. The escape velocity at the separation altitude was 22.4 cm/s , whereas the DCAM3 velocity with respect to the asteroid-centered inertial frame was 13.6 cm/s at the moment of separation. The initial velocity of DCAM3 was approximately 40% below the escape limit, confining its trajectory to a suborbital region.

5.4. Gravity estimation

During the suborbital flight of DCAM3, the altitude remained at a level where the asteroid gravity was three orders of magnitude stronger than the SRP acceleration (see Fig. 20). This situation potentially allows us to extract gravimetric information solely from DCAM3 images. However, the DCAM3 trajectory was not sensitive enough to the asteroid's gravity field to recover higher-order Stokes coefficients. We therefore focus on estimating the standard gravitational parameter, GM , of the asteroid. This section compares the performance of our novel gravity estimation scheme with that of existing ones.

The gravitational parameter of Ryugu was constrained thorough the gravity measurement operation conducted by Hayabusa2. This operation consisted of one set of free-fall and free ascent with a minimum surface altitude of less than 1 km . By compiling radiometric, altimetric, and optical measurements, the gravitational parameter was determined to be $30.0 \pm 0.4 \text{ m}^3/\text{s}^2$ (Watanabe et al., 2019). In a subsequent analysis with additional datasets, this value was updated to $29.8 \pm 0.3 \text{ m}^3/\text{s}^2$ (Yamamoto et al., 2020). Based on these considerations, the current accuracy of GM estimation using Hayabusa2 tracking data is approximately 1%.

In this study, we attempt to independently estimate gravitational parameter without relying on the aforementioned Hayabusa2 data. Fig. 24 illustrates the sensitivity of the fitting residuals to the assumed GM of Ryugu. This diagram compares the x_{AF} components of position residuals for three different gravitational parameters, $20, 30$, and $40 \text{ m}^3/\text{s}^2$. The optimal trajectory that minimizes the least-squares error is solved in each case. The position deviations are normalized using the corresponding standard errors to discern the trend in the residuals. In the nominal case with $GM = 30 \text{ m}^3/\text{s}^2$ shown in the middle panel of Fig. 24, the deviations are uniformly distributed around the zero line, mostly within a range of 2σ . In contrast, the top and bottom panels demonstrate that the fitting residuals notably increase when the assumed gravitational parameter is excessively small ($20 \text{ m}^3/\text{s}^2$) or large

($40 \text{ m}^3/\text{s}^2$). Moreover, these erroneous cases exhibit nonflat residuals that vary with time, suggesting the occurrence of modeling errors in orbital motion under gravity.

As a more quantitative analysis, we simultaneously solve the trajectory of DCAM3 and the gravitational parameter of Ryugu via the least-squares estimation. This analysis corresponds to Step 5, described in Section 3.5.2. The estimated gravitational parameter is $29.2 \text{ m}^3/\text{s}^2$, with a standard error of $1.0 \text{ m}^3/\text{s}^2$. This figure is consistent with the previous estimates cited above within the margin of error. Considering a 3σ error range, the uncertainty of the gravitational parameter derived from DCAM3 images is 10%. The gravimetric accuracy is one order of magnitude lower than that of the gravity measurement conducted by Hayabusa2. Consequently, we ultimately decide to fix the gravitational parameter to the preexisting value ($30 \text{ m}^3/\text{s}^2$) for the DCAM3 orbit determination discussed in this article, except for in this section. The gravitational parameter is treated as a consider parameter with an uncertainty of $0.4 \text{ m}^3/\text{s}^2$ at the 3σ level.

Despite the limited precision of the current estimate, the value of the proposed gravimetric technique remains intact. Even though the mechanical and operational designs of DCAM3 were not optimized for gravity measurement, we managed to determine the gravity of Ryugu with a decent level of uncertainty solely from optical images. The duration and minimum radial distance of the gravity measurement conducted by Hayabusa2 were 21.5 h and $\sim 1.4 \text{ km}$, respectively (Watanabe et al., 2019), while those of the DCAM3 orbit determination data were 1.2 h and 1.25 km , respectively (see Fig. 18). If DCAM3 had been able to obtain asteroid images for a longer period, the gravimetric performance would have been greater. The optical gravimetry approach using small deployable spacecraft established in this paper could improve future small-body missions.

6. Attitude determination

6.1. Reconstructed attitude

The time history of the DCAM3 attitude was reconstructed via the long-term estimation in Step 4, as detailed in Section 3.5.2. The primary parameters pertinent to the estimated attitude are summarized in Table 9. The attitude motion of DCAM3 exhibited spin and nutation, as visualized in Fig. 25. This figure demonstrates that spin motion caused drastic changes in the asteroid orientation with respect to the image plane. Because of the nutation of the optical axis, Ryugu repeatedly entered and exited the field of view at intervals shorter than 10 s . Below is the typical cyclic motion of the asteroid within the field of view: (1) the south pole of the asteroid begins to be captured, (2) the equatorial region, including the SCI crater, enters the field of view, (3) nearly the entire hemisphere becomes observable, (4) the asteroid begins to drift out, with its

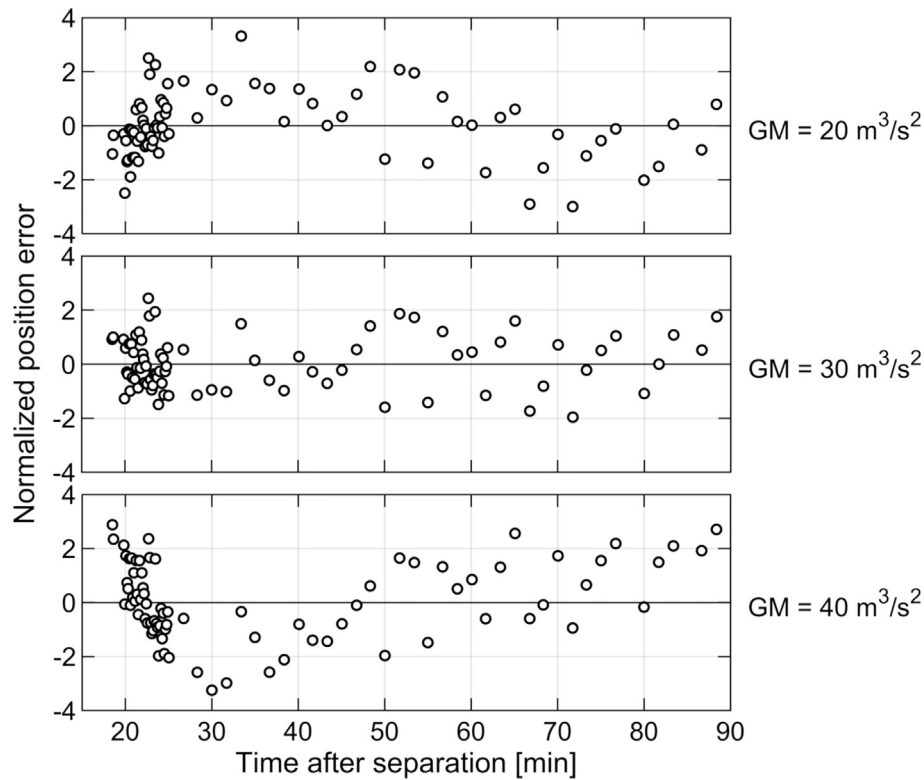


Fig. 24. Residual plots for different gravitational parameters. This figure illustrates the time histories of the normalized position residuals, which are defined as the fitting residuals of the x_{AF} components divided by the corresponding standard errors. The top, middle, and bottom panels show the diagrams for $GM = 20, 30$, and $40 \text{ m}^3/\text{s}^2$, respectively.

Table 9
Primary characteristics of the estimated attitude motion of DCAM3.

Item	Symbol	Value
Nutation angle	γ	28.5 deg
Angular momentum	$ L $	$4.76 \times 10^{-4} \text{ Nms}$
Inertial spin rate	$ \omega $	53.3 deg/s
Inertial nutation rate	ω_n	45.9 deg/s
Relative spin rate	ω_b	8.2 deg/s

equatorial ridge still in view, and (5) the asteroid disappears from the field of view.

The entire profile of the nutation is depicted in Fig. 26. The optical axis nutated around the angular momentum vector with an amplitude of 28.5 deg, which is defined by Eq. (13) as the mean nutation angle. The angular momentum direction was shifted toward the south of the asteroid compared to the ideal orientation, resulting in a situation where the northern hemisphere was less accessible for observation. Fig. 26 indicates that discrete attitude estimates obtained in short-term estimations cover approximately one-third of the nutation phase. As discussed later in Section 6.3, disturbance torque was applied to DCAM3, gradually altering the angular momentum. Nevertheless, this effect was minimal, and thus, no significant precession was evident in the attitude profile shown in Fig. 26.

Fig. 27 depicts the temporal variation in the DCAM3 attitude. Each short-term estimation with a time scale of

1–2 s employs two or three consecutive images to determine the attitude angle and angular velocity at the initial epoch corresponding to the first image. The estimated initial states, represented by filled markers in the left panels, are used to estimate a continuous attitude profile via long-term fitting, whereas instantaneous estimates corresponding to the second and third images are also plotted as open markers, demonstrating overall dynamical consistency. The top left panel indicates that the fluctuations in ϕ and θ (i.e., nutation) and the nonlinear variation in ψ (i.e., spin) are both reconstructed from instantaneous estimates. The estimated angular velocity components are also in good agreement with short-term data points, as demonstrated in the bottom left panel of Fig. 27. According to the right panels, the deviations of the instantaneous estimates from the numerically propagated profiles coincide within the bounds of error in most cases. As summarized in Table 10, the fitting residuals of the Euler angles and angular velocities are less than 0.5 deg and 0.2 deg/s, respectively.

The frequency spectrum derived from the time-domain profile of the attitude quaternion of DCAM3 is presented in Fig. 28. This figure is generated by applying a discrete Fourier transform to the time history of the scalar component of the attitude quaternion. Three clear peaks appear in this plot, which indicates that the attitude motion is governed by these frequencies. Section 3.3 illustrates that the attitude motion of DCAM3 can be analytically approxi-

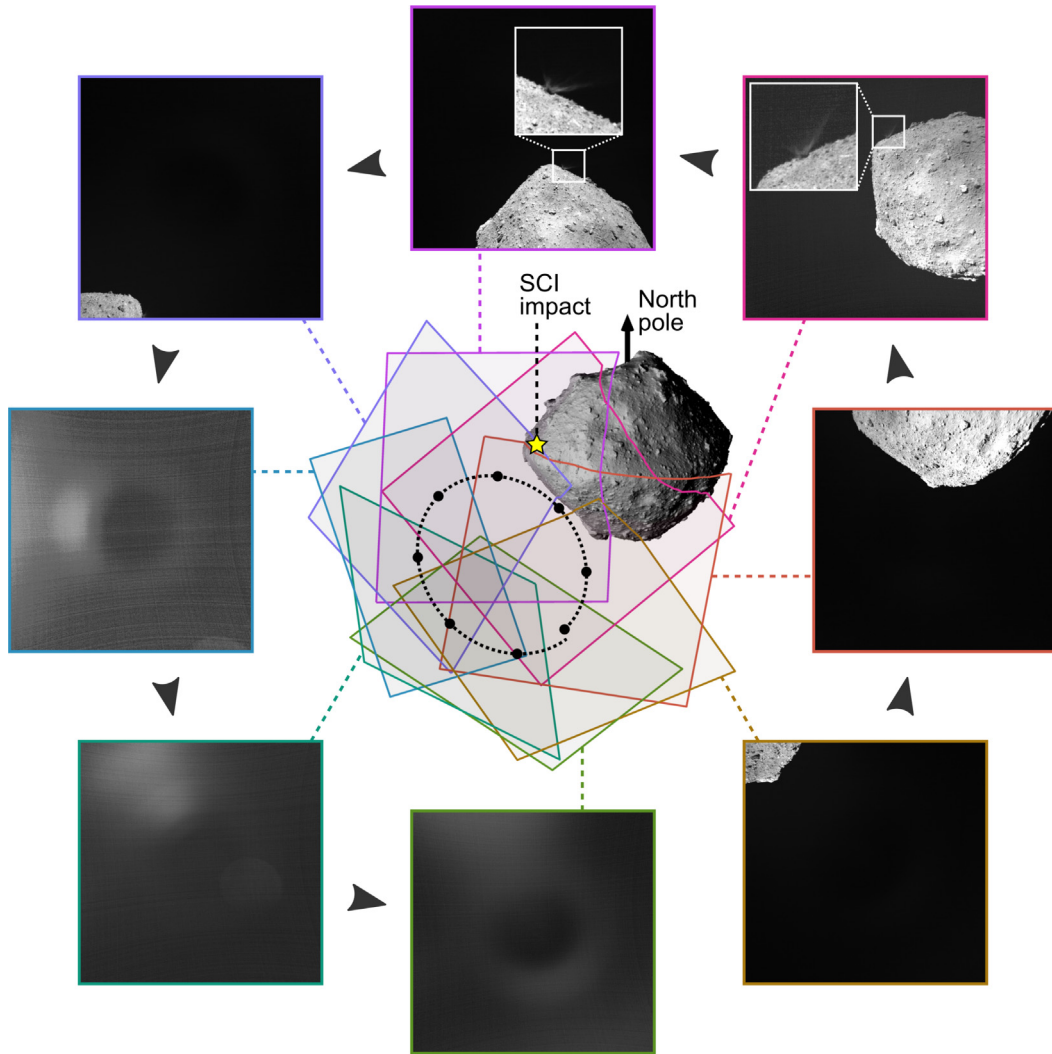


Fig. 25. Short-term variations in the imaging area due to the attitude motion of DCAM3. The center part visualizes the simulated fields of view with respect to the shape model of Ryugu. The dotted elliptical profile illustrates the nutation of DCAM3, with dots indicating the instantaneous locations of the optical axis. The surrounding square windows display DCAM3 images obtained with intervals of ~ 1 s between 1400 and 1407 s after separation. The asteroid is visible in five out of eight images, two of which capture the SCI ejecta curtain.

mated by the torque-free axisymmetric rigid body model. Fig. 28 shows that the three primary frequencies of the numerically computed spectrum match the analytical solutions of the inertial nutation rate ω_n , the relative spin rate ω_b , and their summation. The displayed ω_n and ω_b values show the mean values calculated from Eqs. (14) and (15), respectively. With these numerical and analytical approaches, we determine that the inertial nutation rate and relative spin rate of DCAM3 were 45.9 and 8.2 deg/s, respectively. The former value indicates that the camera's optical axis pointed in approximately the same direction relative to the asteroid at every ~ 8 s, as visualized in Fig. 25. The latter value characterizes the change rate of the direction of the instantaneous spin axis with respect to the image plane, which corresponds to the periodic variation in the distortion profile due to the rolling shutter effect (see Section 4.3).

The inertial spin rate, $|\omega|$, was nearly constant at 53.3 deg/s. The angular momentum of DCAM3 was

approximately conserved owing to its rapid rotation, for which the average value was 4.76×10^{-4} Nms. The angular momentum variation caused by attitude disturbances, which is the primary focus of the subsequent section, was less than 10^{-6} Nms. According to the design specifications for the DCAM3 separation mechanism, the expected spin rate range was 54–132 deg/s (Sawada et al., 2017). The equivalent lower and upper bounds of the angular momentum are 4.53×10^{-4} and 1.11×10^{-3} Nms, respectively, for pure rotation. The actual spin frequency estimated in this study is within the predicted range and close to the lower bound.

By combining the reconstructed attitude and orbit profiles, we can determine the DCAM3 observation geometry. Fig. 29 shows the orientation of the optical axis relative to the asteroid. The angular deviations with respect to the directions of the center of the asteroid and the SCI impact point are depicted. For both directions, the regions

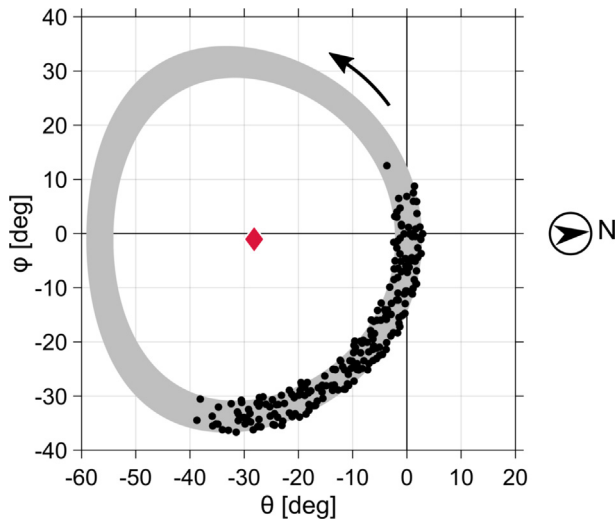


Fig. 26. Estimated nutation motion of the optical axis expressed in the θ - ϕ plane. The dots represent instantaneous estimates of the orientations of the optical axis. The gray shaded region illustrates the area swept out by the nutation motion, whose direction is shown by the arrow. The diamond marker and the circled arrowhead indicate the orientation of the angular momentum vector and the direction of the asteroid's north pole, respectively, at the separation epoch.

bounded by the upper and lower limits encompass the line corresponding to the diagonal field of view. This fact indicates that DCAM3 had intermittent opportunities to capture the asteroid center or SCI crater for at least 1.5h after separation. In particular, within 10 min after SCI detonation, the SCI impact point was sufficiently close to the image center, with a minimum separation angle of 10 deg, allowing for close-up monitoring of SCI impact ejecta. The maximum and minimum separation angles with respect to the center of Ryugu approximately linearly increase at a rate of ~ 17 deg/h. The resulting lack of observed feature points prevents accurate orbit and attitude determination in later periods.

6.2. Moment of inertia

Like with a conventional spacecraft, mechanical tests were conducted for DCAM3 before launch (Sawada et al., 2017). Its inertia properties were, however, not directly measured on the ground because of its miniature size. Instead, the moment of inertia tensor of DCAM3 was calculated using a three-dimensional computer aided design (CAD) model. We anticipate that minor errors in the model, such as the misalignment of wire harnesses, can lead to a few percent error in the moment of inertia. Our attitude determination is sensitive enough to detect such small modeling errors; thus, the moment of inertia values are treated as estimation parameters.

Although the inertia tensor consists of six independent elements, the degree of freedom in our analysis is five. This is because the external torque also serves as a parameter for estimation, leading to indeterminacy in the magnitudes of

torque and the moment of inertia. The ratios of I_{xx} , I_{yy} , I_{xy} , I_{yz} , and I_{xz} with respect to I_{zz} are solved via the least-square method. The absolute scale of these inertia parameters is calculated such that the difference from the original CAD model is minimized.

Table 11 summarizes the estimated inertia parameters. DCAM3 has a nearly axisymmetric shape with $I_{xx} \simeq I_{yy} > I_{zz}$. The products of inertia are two orders of magnitude smaller than the diagonal terms. The deviation from the CAD-based moment of inertia is approximately 2%, which is reasonable considering the potential mis modeling in the prelaunch model described above. The estimated differences are statistically significant according to the uncertainties listed in Table 11. The overall estimation accuracy is as high as $< 0.03\%$. Note that the uncertainties mentioned here pertain to the relative ratios of inertia parameters for the adopted dynamical model, not to their absolute values.

6.3. Attitude disturbance

6.3.1. Continuous disturbance

DCAM3 exhibited nearly torque-free motion owing to its rapid spinning, yet a detectable effect of disturbance torque was still present. This torque was time-variant, and its magnitude was on the order of 10^{-10} – 10^{-9} Nm, which cannot be explained by deterministic environmental disturbances such as the gravity-gradient torque and SRP torque. Hence, we estimated the unmodeled torque in the process of determining the attitude motion. Because the continuous attitude disturbance appeared to be particularly prominent about the optical axis, we considered only the perturbing torque about the z -axis of the camera-fixed frame. The unmodeled torque is expressed as a function of time using a finite Fourier series by the equation below.

$$T(t) = a_0 + \sum_{j=1}^{n_t} (a_j \cos j\omega t + b_j \sin j\omega t), \quad (38)$$

where a_j ($j = 0, \dots, n_t$), b_j ($j = 1, \dots, n_t$), and ω are the parameters to be estimated. The time scale of torque variations that can be expressed by Eq. (38) depends on the degree of the Fourier series. This parameter is set to $n_t = 4$, resulting in a total of ten unknown parameters.

Fig. 30 shows the estimated profile of the unmodeled torque. For comparison, the gravity-gradient torque and SRP torque are computed from Eqs. (11) and (12), respectively, and plotted in Fig. 30. The unmodeled torque reaches up to $\sim 1 \times 10^{-9}$ Nm and demonstrates nonmonotonic time variations. The torque magnitude is comparable to or less than the level of uncertainty at later epochs but is statistically significant at least for the first 40 min after separation. The asteroid gravity and SRP are probably not responsible for the detected torque, given their much smaller magnitudes shown in Fig. 30. Typical examples of such unmodeled torques usually include fuel sloshing and mechanical vibrations of flexible appendages (Hughes,

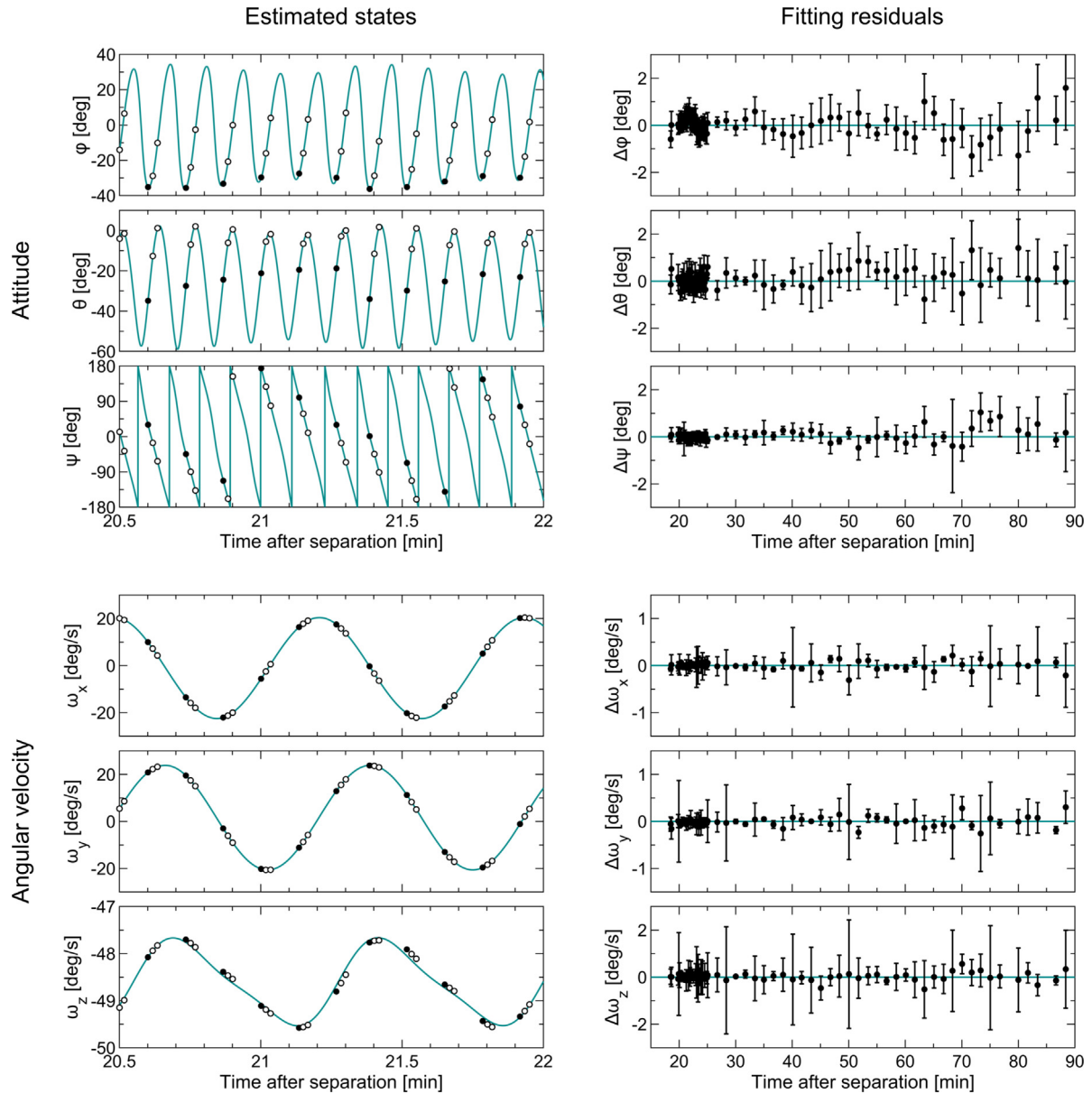


Fig. 27. Temporal variations in the estimated attitude states of DCAM3. The estimated Euler angles (top left), the estimated angular velocities (bottom left), the fitting residuals for Euler angles (top right), and those for angular velocities (bottom right). The dots, curves, and error bars are plotted in the same manner as Fig. 19. The open circles in the left panels represent state parameters corresponding to the second and third images among the sets of two or three images used in short-term estimations. The time scales of the state plots and residual plots are different.

Table 10
Fitting residuals for the attitude angle and angular velocity components.

Parameter	Variable	RMS error
Attitude angle	ϕ	0.450 deg
	θ	0.397 deg
	ψ	0.247 deg
Angular velocity	ω_x	0.074 deg/s
	ω_y	0.085 deg/s
	ω_z	0.150 deg/s

2004), which are not applied in our case. Another candidate for spacecraft-induced torque is outgassing

(Scialdone, 1986); however, given that DCAM3 had been exposed to vacuum conditions for more than four years, this also seems unlikely to be a contributing factor.

One possibility is that dust particles attached to DCAM3 were scattered due to the spin of the camera. We observed that numerous asteroid particles were uplifted during the first touchdown of Hayabusa2, which eventually adhered to the spacecraft and induced degradation in remote-sensing instruments (Morota et al., 2020; Kouyama et al., 2021). Some of these particles remained adhered to the spacecraft until the SCI operation and were detached due to the impulsive disturbance caused by the SCI separation (Ogawa et al., 2022). These observations

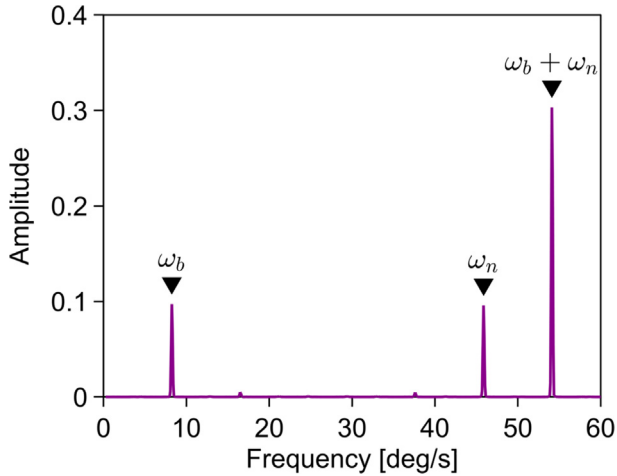


Fig. 28. Frequency spectrum of the attitude motion of DCAM3. The discrete Fourier transform is applied to the numerically calculated profile of the scalar component \hat{q} of the attitude quaternion, converting its time-domain representation into the frequency domain. The triangle markers represent the analytically derived frequencies of the nutation and spin motions.

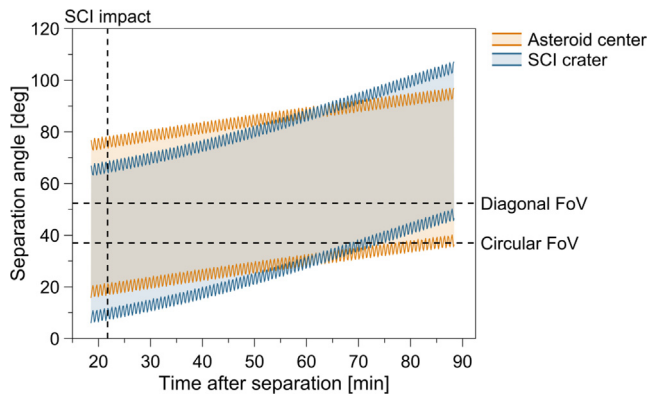


Fig. 29. Time history of the viewing geometry of DCAM3 during the period when the attitude motion is estimated. The separation angles from the optical axis toward the center of the asteroid and toward the SCI impact point are shown. For each parameter, the upper and lower bounds of the separation angle over one nutation period are represented by two sinusoidal curves. The vertical dashed line indicates the time of SCI impact. The two horizontal dashed lines represent the half-angles of the circular and diagonal fields of view (37 and 52 deg, respectively).

Table 11

Estimated moment of inertia of DCAM3. The second column from the right indicates the ratios of the differences from initial CAD-based values to $I_r \equiv (I_{xx} + I_{yy})/2$. The rightmost column shows the 3σ uncertainties in the ratios of the inertia parameters to the I_{zz} value.

Item	Value [kgm^2]	Difference	Uncertainty
I_{xx}	5.97×10^{-4}	−0.383%	0.027%
I_{yy}	5.91×10^{-4}	−1.962%	0.024%
I_{zz}	4.93×10^{-4}	+1.962%	—
I_{xy}	-9.40×10^{-7}	−0.060%	0.014%
I_{yz}	3.29×10^{-6}	+1.227%	0.005%
I_{xz}	-2.24×10^{-6}	+0.640%	0.006%

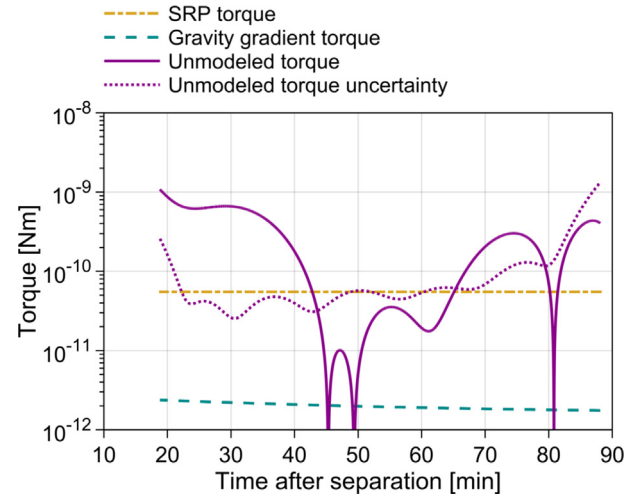


Fig. 30. Comparison of disturbance torques acting on DCAM3. The dot-dashed, dashed, and solid curves show the time histories of the SRP, gravity gradient, and unmodeled torques, respectively, during the period when the attitude motion is estimated. The dotted curve represents the uncertainty, which corresponds to three standard errors, in the estimated unmodeled torque.

suggest that DCAM3 could be covered with dust particles before separation and that the angular momentum of DCAM3 could be transferred into the translational momentum of scattered particles. This scenario is consistent with the fact that the estimated torque acted in the direction that reduces the camera's angular momentum. By integrating the unmodeled torque between 18.5 and 42.5 min after separation, during which the torque magnitude was statistically significant, the total angular impulse was determined to be 8×10^{-7} Nms. Let us assume a pure rotation with a spin rate of 53.3 deg/s for simplicity. The tangential velocity at the lateral surface of DCAM3 is 3.7 cm/s, given an arm length of $d/2 = 4$ cm. Therefore, the mass loss equivalent to the momentum change mentioned above is ~ 0.54 g, which is approximately one tenth of the mass of the returned samples (Yada et al., 2022). This mass-shedding hypothesis holds certain validity; however, the concerns include whether dust particles actually adhered to the DCAM3 unit mounted on the anti-asteroid side and whether the particles could be dispersed continuously rather than instantaneously.

Another plausible cause of the unknown disturbance could be magnetic torque induced by the interplanetary magnetic field. At the heliocentric distance of Ryugu, the magnitude of the interplanetary magnetic field typically falls within 1–10 nT (Behannon, 1978; Ness and Burlaga, 2001). The residual magnetic moment of a small, uncompensated spacecraft can be on the order of 0.1 to 1 Am² (Larson and Wertz, 1999; Sakai et al., 2008; Lassakeur et al., 2018). Simple multiplication yields a magnetic torque range of 10^{-10} – 10^{-8} Nm, which is consistent with the estimated magnitude of the disturbance torque. In addition, the nonmonotonic profile of the detected torque can be

explained by the fact that the interplanetary magnetic field fluctuates on a minute scale. The torque component parallel to the spin axis cancels out in pure rotation (Longuski et al., 1992), but a certain level of torque remains uncompensated for a nutating spacecraft that is not perfectly axisymmetric. Nevertheless, the fact that the torques about the other perpendicular axes remain undetected is a somewhat weak point of this hypothesis.

As the size of a spacecraft decreases, the torques generated by gravity and the SRP diminish. In contrast, magnetic torque does not explicitly depend on the probe dimensions, thereby exerting a relatively significant influence on the attitude motion of spacecraft with small moments of inertia. One past example is the deep-space microspacecraft PROCYON launched along with Hayabusa2 (Funase et al., 2015). This 65-kg spacecraft experienced continuous attitude disturbance, which gravity and the SRP could not account for, about a specific axis during its interplanetary flight (Ikari et al., 2017). The unmodeled torque was on the order of 10^{-8} Nm and was suspected to be the cause of the interplanetary magnetic field. We view this earlier example as supporting evidence for the current discussion on the unaccounted attitude disturbance acting on DCAM3. The growing trend of deep space exploration using small spacecraft is expected to lead to a better understanding of attitude dynamics subject to such minor disturbances.

6.3.2. Impulsive disturbance

A collection of discrete attitude estimates obtained via short-term estimations reveals a small instantaneous change in the attitude profile near the middle of the data arc. The long-term attitude fitting, detailed in Section 6.1, incorporates this effect through an approach described later in this section. Fig. 31 provides an example residual plot for the case where the impulsive disturbance is not accounted for. The error between the discrete estimates and the continuous profile computed via numerical propa-

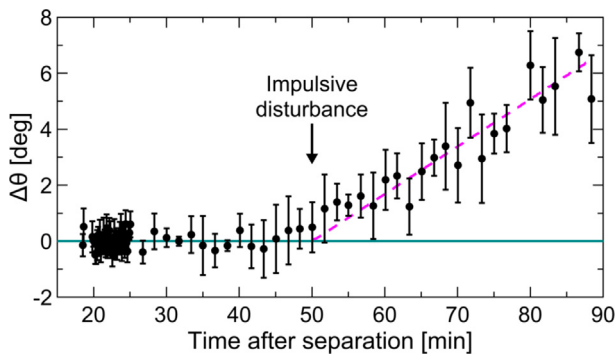


Fig. 31. Residual plot for the Euler angle θ without considering impulsive attitude disturbance. The dots show the differences in the instantaneous estimates from the propagated attitude with no inertia tensor change. The associated error bars indicate 2σ uncertainties. The diagonal dashed line represents the peak profile corresponding to the case with an impulsive disturbance at 50 min after separation.

gation linearly increases from approximately 50 min after separation. Before and after this epoch, the attitude dynamics of DCAM3 can be characterized as nearly torque-free motion, except for the minor continuous disturbance described in the previous section. Note that the angular deviation between the cases with and without the instantaneous perturbing effect appears as a growing oscillation, and the diagonal line in Fig. 31 represents its envelope. This attitude disturbance occurred within a duration much shorter than the temporal scale expressed by Eq. (38). For these reasons, the attitude motion was probably subject to an impulsive disturbance that caused a minor change in attitude behavior. We consider two possible causes of this disturbance: the change in the moment of inertia due to particle adhesion and the angular impulse caused by particle collision.

The former hypothesis is supported by the fact that many particles, presumably lifted during the landing of Hayabusa2, were scattered at the moment of SCI separation. It is reasonable to assume that similar particle detachments could occur upon DCAM3 separation. Reattachment of any of these particles could alter the inertia properties of DCAM3 during the imaging sequence. Let us assume that a small particle with a mass of Δm adheres to the surface of the camera. The resultant change in the moment of inertia is given by the equation below.

$$\Delta \mathbf{I} = \Delta m \begin{bmatrix} y^2 + z^2 & -xy & -zx \\ -xy & x^2 + z^2 & -yz \\ -zx & -yz & x^2 + y^2 \end{bmatrix}, \quad (39)$$

where x , y , and z represent the camera-fixed location of the adhered particle. The mass and position of the particle can be treated as estimation parameters in long-term fitting and can be simultaneously solved with the attitude motion of DCAM3.

The calculation results indicate that the particle was located on the lateral surface of the cylindrical body near its midpoint ($z \simeq 3$ mm). The estimated mass is $\Delta m = 74.3 \pm 1.6$ mg, where the uncertainty represents one standard error. According to onground sample analyses, the mean bulk density of returned asteroid particles with sizes of 1–8 mm is 1.8 g/cm^3 (Nakamura et al., 2022). Therefore, the diameter of the adhered particle is estimated to be ~ 4 mm, assuming an ideal spherical shape. This figure is comparable to the sizes of the samples collected by Hayabusa2 and of the particles attached to the spacecraft (Yada et al., 2022; Morota et al., 2020). It is intriguing that even such a small particle could have a detectable impact on the attitude dynamics of DCAM3. Although further investigation of the reattachment mechanism is imperative, this particle adhesion scenario can provide one plausible explanation for the impulsive attitude disturbance.

On the other hand, the particle collision hypothesis can be attributed to either a fragment of SCI or an asteroid particle ejected by the SCI impact. A colliding particle must reach the DCAM3 location from either the SCI detonation

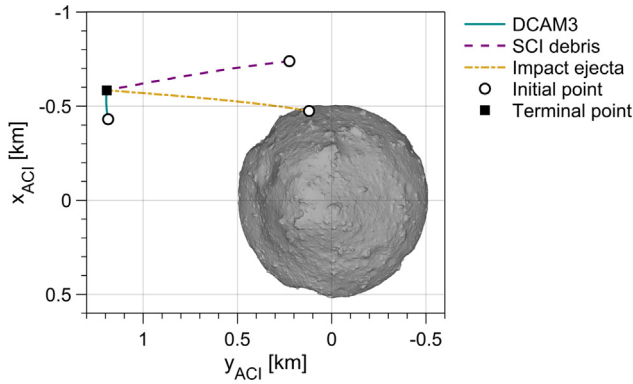


Fig. 32. Trajectories of SCI debris and impact ejecta potentially colliding with DCAM3. The solid, dashed, and dot-dashed curves represent the trajectories of DCAM3, an impactor fragment, and an ejecta particle, respectively. The circle markers indicate the locations of these three objects at the time of SCI impact, which occurred 21.8 min after DCAM3 separation. The square marker corresponds to the terminal epoch, 50.0 min after separation, where impulsive attitude disturbance was applied.

Table 12

Possible ejection and impact conditions of an SCI fragment and an ejecta particle based on trajectory analyses. The ejection angles of an SCI fragment and an ejecta particle are defined with respect to the hypothetical plane normal to the firing direction of the SCI projectile and with respect to the local horizontal at the SCI impact point, respectively. The ejection velocity is expressed in the asteroid-centered inertial frame. The impact velocity is defined as the velocity of a colliding object relative to the velocity of DCAM3.

Object	Ejection angle	Ejection velocity	Impact velocity
SCI fragment	−19.4 deg	59.8 cm/s	59.5 cm/s
Ejecta particle	12.2 deg	68.0 cm/s	62.2 cm/s

point above the asteroid or the SCI impact point on the asteroid surface. The initial epoch at which SCI detonated itself corresponds to 21.8 min after DCAM3 separation, while the terminal epoch at which the particle collided corresponds to ~ 50 min after DCAM3 separation. Because the initial and terminal positions are given, possible trajectories of the impacting particle can be numerically solved as two-point boundary value problems. Fig. 32 shows the possible impact trajectories of an SCI fragment and ejecta particle, and Table 12 summarizes the corresponding ejection and impact conditions.

Because the flight times are identical in both cases, the particles' impact velocities take similar values of ~ 0.6 m/s. The instantaneous momentum change estimated from DCAM3 images is approximately 9×10^{-7} Nms, although this change can vary depending on the exact impact timing. As a representative case, let us assume perfectly inelastic collision with an arm length equal to a quarter of the camera's height ($h/4 \simeq 2$ cm). Given the aforementioned impact velocity and momentum variation, the mass of a colliding particle is approximately 75 mg. As discussed for the particle adhesion hypothesis, this mass approximately corresponds to a spherical asteroid particle

with a diameter of ~ 4 mm. Our result agrees with previous findings that the sizes of ejecta particles produced by the SCI impact ranged from 1 mm to several decimeters (Wada et al., 2021). However, the ejection angle needed for a particle to reach DCAM3 from the asteroid is as small as 12.2 deg. This value deviates considerably from the typical ejection angle of 45 deg and appears to be inconsistent with the actual shape of the SCI ejecta curtain (Kadono et al., 2020; Wada et al., 2021). For a similar reason, the collision of SCI debris is questionable. As shown in Table 12, the ejection angle of an impactor fragment must be negative to reach the DCAM3 trajectory, indicating that this fragment should be scattered backward relative to the firing direction of the SCI projectile. In contrast, onground experiments have demonstrated that SCI debris predominantly scatters forward (Shimaki et al., 2021). Nevertheless, the attitude of DCAM3 could still have been disturbed due to particles ejected by the impact of an SCI fragment or particles deflected by a boulder after ejection.

Although the possibility of particle collision cannot be ruled out, we attributed the impulsive attitude disturbance to the change in the inertia tensor caused by particle adhesion. Attitude analyses relying solely on DCAM3 images are insufficient for distinguishing between these two scenarios. However, this limitation does not compromise the quality of the derived attitude solution. The estimated attitude motion, subject to impulsive disturbance, agrees with DCAM3 observations (see Fig. 27). Hence, the reconstruction of the DCAM3-Ryugu geometry remains reliable.

6.4. Attitude refinement

The continuous attitude motion of DCAM3 was successfully reconstructed via nonlinear fitting, providing insights into the general patterns of shifts in the camera's field of view. However, it is not necessarily promising to precisely determine the instantaneous camera orientations that perfectly follow the attitude dynamics model. This is partly due to the high frequency of the attitude motion, which is approximately 50 deg/s according to Fig. 28. Given that there is at least 1 ms of ambiguity in the imaging epochs, the dynamic attitude model cannot ascertain the camera orientation with more than 0.05 deg of accuracy. This level of uncertainty exceeds the pixel scale of DCAM3 (0.615 mrad). In addition, Fig. 30 indicates that the estimation uncertainty of the unmodeled torque is on the order of 10^{-10} Nm. The moment of inertia about the central axis is $\sim 5 \times 10^{-4}$ kgm², leading to uncertainty in angular acceleration on the order of 10^{-5} deg/s². Consequently, in the case of low-frequency observations with time intervals of ~ 100 s, attitude estimation relying on the adopted torque model could incur an error of up to ~ 0.5 deg.

To refine the DCAM3 orientation information, we slightly adjust the instantaneous attitude angles via feature matching without considering any dynamics. In this final refinement, the positions and image distortion coefficients

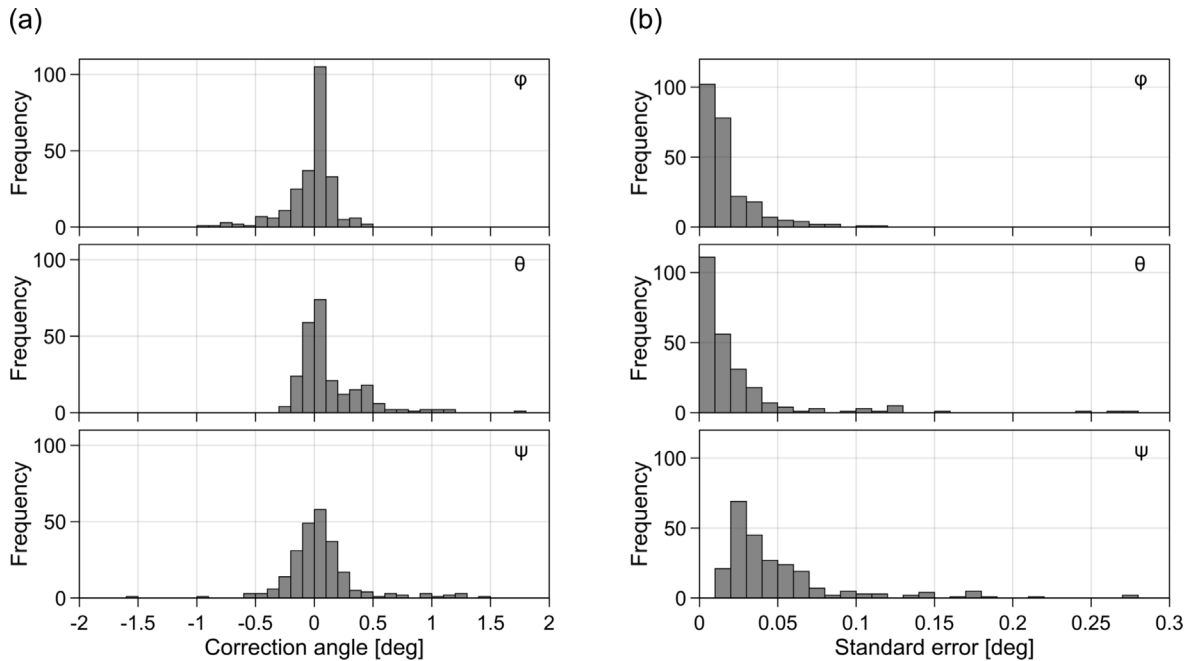


Fig. 33. Statistical results of the final attitude refinement. Histograms for (a) the angular corrections and (b) the standard errors of the refined attitudes. Three outliers exist for ϕ and four outliers exist for ψ outside the angular range shown in panel (b).

of DCAM3 are fixed to the values obtained from nonlinear fitting (see Table 4). This process is of particular importance for characterizing the dynamic evolution of SCI impact ejecta based on precise information about DCAM3 observation geometries (Kikuchi et al., 2023). A total of 245 DCAM3 images are analyzed to determine the instantaneous attitude states.

Fig. 33(a) shows the differences between the updated attitude estimates obtained in the final refinement and the original attitude estimates obtained through long-term fitting. The angle corrections for each Euler angle are less than 0.5 deg in most cases, and the RMS errors are 0.2–0.3 deg. This observation indicates that the initial long-term solutions are close to the final optimal values. The adopted small adjustment absorbed the uncertainty in the dynamics model.

The expected accuracy of the refined attitude angles can be characterized by covariance matrices associated with feature matching. Fig. 33(b) depicts the distribution of the standard errors of the instantaneous attitudes estimated in the final refinement. The histograms for the optical axis orientation, ϕ and θ , have similar profiles, and the histogram for the spin phase, ψ , shows larger errors. The 90th percentile values of the standard errors of ϕ and θ are ~ 0.04 deg, and that of ψ is ~ 0.11 deg. The former value is approximately equivalent to the instantaneous field of view of 0.615 mrad. The latter error, when converted into pixel deviation in the middle of the field of view (i.e., at 500 px from the optical center), equals approximately 1 px. We therefore conclude that the geometric relationship between DCAM3 and Ryugu has been reconstructed with a sufficiently high accuracy comparable to the camera's pixel scale.

7. Conclusion

We simultaneously completed geometric calibration and orbit and attitude determination of DCAM3 using optical images obtained by DCAM3 itself. To address the large-scale problem with many observables and estimation parameters, the analysis was conducted through a stepwise least-squares approach, primarily consisting of short-term and long-term estimations. For each short-term analysis, a set of two or three consecutive DCAM3 images with a time interval of 1 s was utilized to estimate the instantaneous position and attitude of DCAM3 as well as the image distortion profile. The discrete position and attitude estimates were subsequently used in the batch estimations of the long-term continuous orbital and attitude motions.

The geometric relationship between DCAM3 and Ryugu was reconstructed by matching feature points captured in DCAM3 images with those in ONC-T images whose three-dimensional locations are given. A total of 969 unique feature points were used in short-term estimations, leading to the cumulative number of observed feature points exceeding 10,000. By simultaneously estimating the camera's position, orientation, and distortion at each imaging epoch, the pixel locations of feature points were precisely reproduced with typical reprojection errors of 0.5–1.5 px. The lens distortion coefficients k_1 , k_2 , and k_3 were determined with standard errors of 0.5%, 1.6%, and 3.0%, respectively, which corresponds to the modeling accuracy of ~ 1 px at the edge of the image plane. The time-varying distortion caused by the rolling shutter effect was precisely computed based on the DCAM3 attitude numerically integrated with a time interval of 5 ms. Despite the combination of these two effects resulting in complex distortions up to 400 px, geometric

calibration was successfully achieved by applying an inverse operation.

The trajectory of DCAM3 was reconstructed as an optimal solution that best fit discrete position estimates obtained from its optical data. The positional uncertainty evaluated at the DCAM3 separation point was less than 0.8 m (1σ) for each axis, approximately equal to the pixel resolution of the camera. The estimation results indicated that DCAM3 followed a semielliptical trajectory and performed suborbital flight for approximately 380 min. The radial distance from the asteroid center was 1.2 km at the separation point and reached a maximum of 1.4 km. During the observation of SCI ejecta, DCAM3 flew at a distance of 1.0–1.1 km from the SCI crater, yielding spatial resolutions of 0.6–0.7 m/px. The camera presumably impacted near the equatorial ridge at a velocity of ~ 40 cm/s after its primary batteries were depleted. The separation performance was subsequently evaluated based on the reconstructed trajectory, revealing a positional deviation of 28.7 m, a directional deviation of 6.5 deg, and a separation velocity of 72.7 cm/s. These results were all within the expected range of the mechanical and operational design of DCAM3. We also demonstrated optical gravimetry using DCAM3 images by treating the gravitational parameter of Ryugu as an estimation parameter. The estimated value of $29.2 \pm 1.0 (1\sigma) \text{ m/s}^2$ was consistent with but less accurate than previous estimates; hence, this parameter was eventually fixed as a consider parameter.

Long-term attitude fitting was performed using image-based instantaneous estimates in the same manner as orbit determination. The attitude of DCAM3 was stabilized by spin torque applied upon separation, and its inertial spin rate was determined to be 53.3 deg/s on average. The attitude motion exhibited nutation with an amplitude of 28.5 deg and an inertial rate of 45.9 deg/s. We demonstrated that the numerically propagated attitude profile can be well characterized by the analytical model for torque-free motion of an axisymmetric rigid body. The SCI crater region was captured within the field of view of DCAM3 as expected, with a minimum separation angle of approximately 10 deg from the optical center. The moment of inertia tensor of DCAM3 was simultaneously adjusted in the attitude determination process, which revealed a slight deviation of approximately 2% compared to the original CAD model. The discrete attitude estimates suggested the effects of continuous and impulsive disturbances. Although the disturbance sources could not be uniquely identified among several possible causes, these unmodeled disturbances were directly estimated, yielding a long-term attitude solution that agrees with short-term discrete estimates. After the final attitude refinement, the orientation of DCAM3 at each observation epoch was determined primarily with an accuracy of ~ 0.04 deg for the optical axis direction and ~ 0.11 deg for the spin phase. These uncertainties are approximately equivalent to the pixel scale of DCAM3 images.

As a result, high-fidelity geometric models for imaging conditions and image calibration were established. The extracted information is imperative for characterizing the three-dimensional shape of the SCI ejecta curtain and its dynamic evolution. Moreover, this study evaluated the performance of the DCAM3 operation, demonstrating the validity of the deployable camera system for future applications. The distinctive aspect of the proposed approach is the derivation of comprehensive dynamical information solely from optical images captured by a subkilogram spacecraft. Consequently, this research will further contribute to facilitating small-body exploration by leveraging small-satellite technology.

Declaration of Competing Interest

The authors declare that they have no known competing financial interests or personal relationships that could have appeared to influence the work reported in this paper.

Acknowledgments

This work was supported by JSPS KAKENHI Grant No. JP23K17710.

Appendix A. SRP force and torque models

The analytical models for the SRP force and torque exerted on DCAM3, which is modeled as a cylinder with ideal Lambertian surfaces, are derived in this section. Solar photons impinging on a surface element dA produce an external force given by the equation below (McInnes, 1999).

$$dF_p = \begin{cases} -\Phi(\mathbf{n} \cdot \mathbf{s}) \left[\{2(\mathbf{n} \cdot \mathbf{s})C_s + \frac{2}{3}C_d\} \mathbf{n} + (C_d + C_a)\mathbf{s} \right] dA & (\mathbf{n} \cdot \mathbf{s} \geq 0) \\ \mathbf{0} & (\mathbf{n} \cdot \mathbf{s} < 0) \end{cases} \quad (40)$$

where Φ is the magnitude of the SRP depending on the solar distance, \mathbf{n} is a unit vector normal to the surface element, and \mathbf{s} is a unit vector pointing from the surface element to the sun. The optical properties are characterized by three constants, C_s , C_d , and C_a , which correspond to specular reflection, diffuse reflection, and absorption, respectively, and satisfy $C_s + C_d + C_a = 1$. The resultant force and torque acting on the cylinder can be calculated by integrating over the surface, as follows:

$$\mathbf{F}_p = \int d\mathbf{F}_p, \quad \mathbf{T}_p = \int \boldsymbol{\rho} \times d\mathbf{F}_p, \quad (41)$$

where $\boldsymbol{\rho}$ denotes the position vector of the surface element dA with respect to the center of mass of the cylinder.

Let us define the body-fixed frame as sketched in Fig. 34. The z -axis is aligned with the central axis of the cylinder. Let α and β be the incidence and azimuth angles, respectively, to describe the direction of the sun with respect to the cylinder. These angles are defined such that the sun

Appendix B. Supplementary material

Supplementary data associated with this article can be found, in the online version, at <https://doi.org/10.1016/j.asr.2024.04.057>.

References

- Ait-Aider, O., Bartoli, A., Andreff, N., 2007. Kinematics from lines in a single rolling shutter image. In: 2007 IEEE Conference on Computer Vision and Pattern Recognition. IEEE. <https://doi.org/10.1109/CVPR.2007.383119>.
- Arakawa, M., Saiki, T., Wada, K., Ogawa, K., Kadono, T., Shirai, K., Sawada, H., Ishibashi, K., Honda, R., Sakatani, N., et al., 2020. An artificial impact on the asteroid (162173) Ryugu formed a crater in the gravity-dominated regime. *Science* 368, 67–71. <https://doi.org/10.1126/science.aaz1701>.
- Behannon, K.W., 1978. Heliocentric distance dependence of the interplanetary magnetic field. *Rev. Geophys.* 16, 125–145. <https://doi.org/10.1029/RG016i001p00125>.
- Bibring, J.P., Rosenbauer, H., Boehnhardt, H., Ulamec, S., Biele, J., Espinasse, S., Feuerbacher, B., Gaudon, P., Hemmerich, P., Kletzkine, P., et al., 2007. The ROSETTA lander ("PHILAE") investigations. *Space Sci. Rev.* 128, 205–220. <https://doi.org/10.1007/s11214-006-9138-2>.
- Bradski, G., Kaehler, A., 2008. *Learning OpenCV: Computer vision with the OpenCV library*, 1st edition. O'Reilly Media Inc, Sebastopol, CA.
- Brown, L.G., 1992. A survey of image registration techniques. *ACM Comput. Surv. (CSUR)* 24, 325–376. <https://doi.org/10.1145/146370.146374>.
- Çelik, O., Baresi, N., Ballouz, R.L., Ogawa, K., Wada, K., Kawakatsu, Y., 2019. Ballistic deployment from quasi-satellite orbits around Phobos under realistic dynamical and surface environment constraints. *Planet. Space Sci.* 178, 104693. <https://doi.org/10.1016/j.pss.2019.06.010>.
- Dotto, E., Della Corte, V., Amoroso, M., Bertini, I., Brucato, J., Capannolo, A., Cotugno, B., Cremonese, G., Di Tana, V., Gai, I., et al., 2021. LICIACube-the Light Italian Cubesat for Imaging of Asteroids in support of the NASA DART mission towards asteroid (65803) Didymos. *Planet. Space Sci.* 199, 105185. <https://doi.org/10.1016/j.pss.2021.105185>.
- Ernst, C.M., Daly, R.T., Gaskell, R.W., Barnouin, O.S., Nair, H., Hyatt, B.A., Al Asad, M.M., Hoch, K.K., 2023. High-resolution shape models of Phobos and Deimos from stereophotoclinometry. *Earth, Planets and Space* 75, 103. <https://doi.org/10.1186/s40623-023-01814-7>.
- Ferrari, F., Franzese, V., Pugliatti, M., Giordano, C., Toppo, F., 2021. Preliminary mission profile of Hera's Milani CubeSat. *Adv. Space Res.* 67, 2010–2029. <https://doi.org/10.1016/j.asr.2020.12.034>.
- Fischler, M.A., Bolles, R.C., 1981. Random sample consensus: a paradigm for model fitting with applications to image analysis and automated cartography. *Commun. ACM* 24, 381–395. <https://doi.org/10.1145/358669.358692>.
- Funase, R., Inamori, T., Ikari, S., Ozaki, N., Koizumi, H., 2015. Initial operation results of a 50kg-class deep space exploration micro-spacecraft PROCYON. In: 29th Annual AIAA/USU Conference on Small Satellites. SSC15-V-5.
- Garmier, R., Torres, A., Martin, T., Lorda, L., Canalias, E., Moussi, A., Biele, J., Scholten, F., Jaumann, R., Ho, T.M., et al., 2021. Attitude reconstruction of MASCOT lander during its descent and stay on asteroid (162173) Ryugu. *Planet. Space Sci.* 195, 105150. <https://doi.org/10.1016/j.pss.2020.105150>.
- Goldberg, H.R., Karatekin, Ö., Ritter, B., Herique, A., Tortora, P., Prioroc, C., Gutierrez, B.G., Martino, P., Carnelli, I., 2019. The Juventas CubeSat in Support of ESA's Hera Mission to the Asteroid Didymos. In: 33rd Annual AIAA/USU Conference on Small Satellites. SSC19-WKIV-05.
- Hapke, B., 2012. *Theory of reflectance and emittance spectroscopy*. Cambridge University Press.
- Heikkilä, J., Silvén, O., 1997. A four-step camera calibration procedure with implicit image correction, in: Proceedings of IEEE computer society conference on computer vision and pattern recognition, IEEE. pp. 1106–1112. [doi:10.1109/CVPR.1997.609468](https://doi.org/10.1109/CVPR.1997.609468).
- Heinisch, P., Auster, H.U., Richter, I., Hercik, D., Jurado, E., Garmier, R., Güttler, C., Glassmeier, K.H., 2016. Attitude reconstruction of ROSETTA's Lander PHILAE using two-point magnetic field observations by ROMAP and RPC-MAG. *Acta Astronaut.* 125, 174–182. <https://doi.org/10.1016/j.actaastro.2015.12.002>.
- Ho, T.M., Baturkin, V., Grimm, C., Grundmann, J.T., Hobbie, C., Ksenik, E., Lange, C., Sasaki, K., Schlotterer, M., Talapina, M., et al., 2017. MASCOT—the mobile asteroid surface scout onboard the Hayabusa2 mission. *Space Sci. Rev.* 208, 339–374. <https://doi.org/10.1007/s11214-016-0251-6>.
- Hughes, P.C., 2004. *Spacecraft Attitude Dynamics*. Dover Publications.
- Ikari, S., Sakagami, R., Matsushita, S., Funase, R., Ito, T., Inamori, T., 2017. Analysis of in-orbit attitude disturbances for the deep-space micro-spacecraft PROCYON [translated from Japanese]. In: Proceedings of the 14th Spacecraft Environment Symposium (in Japanese), pp. 15–28.
- Ishibashi, K., Shirai, K., Ogawa, K., Wada, K., Honda, R., Arakawa, M., Sakatani, N., Ikeda, Y., 2017. Performance of Hayabusa2 DCAM3-D camera for short-range imaging of SCI and ejecta curtain generated from the artificial impact crater formed on asteroid 162137 Ryugu (1999 JU3). *Space Sci. Rev.* 208, 213–238.
- Janson, S., 2011. 25 Years of Small Satellites, in: 25th Annual AIAA/USU Conference on Small Satellites. SSC11-III-1.
- Jurado, E., Martin, T., Canalias, E., Blazquez, A., Garmier, R., Ceolin, T., Gaudon, P., Delmas, C., Biele, J., Ulamec, S., et al., 2016. Rosetta lander Philae: Flight Dynamics analyses for landing site selection and post-landing operations. *Acta Astronaut.* 125, 65–79. <https://doi.org/10.1016/j.actaastro.2016.03.030>.
- Kadono, T., Arakawa, M., Honda, R., Ishibashi, K., Ogawa, K., Sakatani, N., Sawada, H., Shimaki, Y., Shirai, K., Sugita, S., et al., 2020. Impact experiment on asteroid (162173) Ryugu: Structure beneath the impact point revealed by in situ observations of the ejecta curtain. *Astrophys. J. Lett.* 899, L22. <https://doi.org/10.3847/2041-8213/aba949>.
- Kameda, S., Suzuki, H., Takamatsu, T., Cho, Y., Yasuda, T., Yamada, M., Sawada, H., Honda, R., Morota, T., Honda, C., et al., 2017. Preflight calibration test results for optical navigation camera telescope (ONC-T) onboard the Hayabusa2 spacecraft. *Space Sci. Rev.* 208, 17–31. <https://doi.org/10.1007/s11214-015-0227-y>.
- Kaula, W.M., 1966. *Theory of satellite geodesy. Applications of satellites to geodesy*. Waltham.
- Kikuchi, S., Howell, K.C., Tsuda, Y., Kawaguchi, J., 2017. Orbit-attitude coupled motion around small bodies: Sun-synchronous orbits with Sun-tracking attitude motion. *Acta Astronaut.* 140, 34–48. <https://doi.org/10.1016/j.actaastro.2017.07.043>.
- Kikuchi, S., Terui, F., Ogawa, N., Saiki, T., Ono, G., Yoshikawa, K., Takei, Y., Mimasu, Y., Ikeda, H., Sawada, H., et al., 2020. Design and reconstruction of the Hayabusa2 precision landing on Ryugu. *J. Spacecr. Rock.* 57, 1033–1060. <https://doi.org/10.2514/1.A34683>.
- Kikuchi, S., Wada, K., Shirai, K., Ishibashi, K., Kadono, T., Honda, R., Yokota, Y., Shimaki, Y., Sakatani, N., Ogawa, K., Sawada, H., Arakawa, M., 2023. Ejecta plume evolution observed in the Hayabusa2 impact experiment on Ryugu, in: Japan Geoscience Union Meeting 2023. PPS03-20.
- Kikuchi, S., Watanabe, S., Wada, K., Saiki, T., Yabuta, H., Sugita, S., Abe, M., Arakawa, M., Cho, Y., Hayakawa, M., et al., 2022. Site selection for the hayabusa2 artificial cratering and subsurface material sampling on ryugu. *Planet. Space Sci.* 219, 105519. <https://doi.org/10.1016/j.pss.2022.105519>.

- Kouyama, T., Tatsumi, E., Yokota, Y., Yumoto, K., Yamada, M., Honda, R., Kameda, S., Suzuki, H., Sakatani, N., Hayakawa, M., et al., 2021. Post-arrival calibration of Hayabusa2's optical navigation cameras (ONCs): Severe effects from touchdown events. *Icarus* 360, 114353. <https://doi.org/10.1016/j.icarus.2021.114353>.
- Larson, W.J., Wertz, J.R., 1999. *Space mission analysis and design*, third edition. Springer.
- Lassakeur, A., Underwood, C., Taylor, B., 2018. Enhanced attitude stability and control for CubeSats by real-time on-orbit determination of their dynamic magnetic moment, in: 69th International Astronautical Congress. IAC-18-E2.4.1.
- Longuski, J.M., Todd, R.E., Konig, W.W., 1992. Survey of nongravitational forces and space environmental torques-Applied to the Galileo. *Journal of guidance, control, and dynamics* 15, 545–553. <https://doi.org/10.2514/3.20874>.
- Lowe, D.G., 1999. Object recognition from local scale-invariant features. In: *Proceedings of the Seventh IEEE International Conference on Computer Vision*, pp. 1150–1157. <https://doi.org/10.1109/ICCV.1999.790410>.
- Lubey, D.P., Smith, M., Mages, D., Hollenberg, C., Bhaskaran, S., 2023. Navigation Results and Analysis for the LICIA Cube Mission, in: 2023 AAS/AIAA Astrodynamics Specialist Conference. AAS 23–488.
- Magerand, L., Bartoli, A., Ait-Aider, O., Pizarro, D., 2012. Global optimization of object pose and motion from a single rolling shutter image with automatic 2d–3d matching, in: *Computer Vision—ECCV 2012: 12th European Conference on Computer Vision*, Florence, Italy, October 7–13, 2012, *Proceedings, Part I* 12, Springer. pp. 456–469. doi:10.1007/978-3-642-33718-5_33.
- McInnes, C., 1999. *Solar Sailing: Technology, Dynamics and Mission Applications*. Springer.
- McMahon, J., Scheeres, D., Hesar, S., Farnocchia, D., Chesley, S., Lauretta, D., 2018. The OSIRIS-REx radio science experiment at Bennu. *Space Sci. Rev.* 214, 43. <https://doi.org/10.1007/s11214-018-0480-y>.
- Montenbruck, O., Gill, E., 2000. *Satellite Orbits: Models, Methods, and Applications*. Springer Science & Business Media.
- Morota, T., Sugita, S., Cho, Y., Kanamaru, M., Tatsumi, E., Sakatani, N., Honda, R., Hirata, N., Kikuchi, H., Yamada, M., et al., 2020. Sample collection from asteroid (162173) Ryugu by Hayabusa 2: Implications for surface evolution. *Science* 368, 654–659. <https://doi.org/10.1126/science.aaz6306>.
- Nakamura, T., Matsumoto, M., Amano, K., Enokido, Y., Zolensky, M., Mikouchi, T., Genda, H., Tanaka, S., Zolotov, M., Kurosawa, K., et al., 2022. Formation and evolution of carbonaceous asteroid Ryugu: Direct evidence from returned samples. *Science* 379, eabn8671. <https://doi.org/10.1126/science.abn8671>.
- Nelles, O., 2001. *Nonlinear System Identification: From Classical Approaches to Neural Networks and Fuzzy Models*. Springer.
- Ness, N.F., Burlaga, L.F., 2001. Spacecraft studies of the interplanetary magnetic field. *Journal of Geophysical Research: Space Physics* 106, 15803–15817. <https://doi.org/10.1029/2000JA000118>.
- Ogawa, K., Shirai, K., Sawada, H., Arakawa, M., Honda, R., Wada, K., Ishibashi, K., Iijima, Y.i., Sakatani, N., Nakazawa, S., et al., 2017. System configuration and operation plan of Hayabusa2 DCAM3-D camera system for scientific observation during SCI impact experiment. *Space Sci. Rev.* 208, 125–142. <https://doi.org/10.1007/s11214-017-0347-7>.
- Ogawa, N., Yokota, Y., Yumoto, K., Tatsumi, E., Kouyama, T., Morota, T., Yamada, M., Hosoda, S., Tsukizaki, R., Nishiyama, K., et al., 2022. Sensitivity degradation of optical navigation camera and attempts for dust removal, in: *Hayabusa2 Asteroid Sample Return Mission*. Elsevier, pp. 415–431. doi:10.1016/B978-0-323-99731-7.00021-0.
- Saiki, T., Mimasu, Y., Takei, Y., Yamada, M., Sawada, H., Ogawa, K., Ogawa, N., Takeuchi, H., Miura, A., Shimaki, Y., et al., 2020. Motion reconstruction of the small carry-on impactor aboard Hayabusa2. *Astrodynamics* 4, 289–308. <https://doi.org/10.1007/s42064-020-0077-6>.
- Saiki, T., Takei, Y., Mimasu, Y., Sawada, H., Ogawa, N., Ono, G., Yoshikawa, K., Terui, F., Arakawa, M., Sugita, S., et al., 2020. Hayabusa2's kinetic impact experiment: Operational planning and results. *Acta Astronaut.* 175, 362–374. <https://doi.org/10.1016/j.actaastro.2020.05.064>.
- Sakai, S.i., Fukushima, Y., Saito, H., 2008. Design and on-orbit evaluation of magnetic attitude control system for the “REIMEI” microsatellite. In: 2008 10th IEEE International Workshop on Advanced Motion Control. IEEE, pp. 584–589. <https://doi.org/10.1109/AMC.2008.4516132>.
- Sawada, H., Mori, O., Okuizumi, N., Shirasawa, Y., Miyazaki, Y., Natori, M., Matunaga, S., Furuya, H., Sakamoto, H., 2011. Mission report on the solar power sail deployment demonstration of IKAROS, in: 52nd AIAA/ASME/ASCE/AHS/ASC Structures, Structural Dynamics and Materials Conference. AIAA 2011–1887.
- Sawada, H., Ogawa, K., Shirai, K., Kimura, S., Hiromori, Y., Mimasu, Y., DCAM3 Development Team, 2017. Deployable Camera (DCAM3) system for observation of Hayabusa2 impact experiment. *Space Science Reviews* 208, 143–164. doi:10.1007/s11214-017-0337-9.
- Scheeres, D.J., 2012. *Orbital Motion in Strongly Perturbed Environments: Applications to Asteroid, Comet and Planetary Satellite Orbiters*. Springer.
- Scholten, F., Preusker, F., Elgner, S., Matz, K.D., Jaumann, R., Biele, J., Hercik, D., Auster, H.U., Hamm, M., Grott, M., et al., 2019. The descent and bouncing path of the Hayabusa2 lander MASCOT at asteroid (162173) Ryugu. *Astronomy & Astrophysics* 632, L3. <https://doi.org/10.1051/0004-6361/201936757>.
- Scialdone, J.J., 1986. An estimate of the outgassing of space payloads and its gaseous influence on the environment. *Journal of Spacecraft and Rockets* 23, 373–378. <https://doi.org/10.2514/3.25815>.
- Seber, G.A., Wild, C.J., 2003. *Nonlinear regression*. John Wiley & Sons.
- Shimaki, Y., Yokota, Y., Honda, R., Arakawa, M., Wada, K., Kadono, T., Shirai, K., Ogawa, K., Sakatani, N., Ishibashi, K., et al., 2021. Ryugu's surface change formed by SCI forward debris, in: *Japan Geoscience Union Meeting 2021*. PPS03-P04.
- Stacey, N., Dennison, K., D'Amico, S., 2022. Autonomous asteroid characterization through nanosatellite swarming. In: 2022 IEEE Aerospace Conference. IEEE.
- Sugita, S., Honda, R., Morota, T., Kameda, S., Sawada, H., Yokota, Y., Yamada, M., Kouyama, T., Tatsumi, E., Suzuki, H., et al., 2022. Hayabusa2 ONC Bundle. JAXA Data Archives and Transmission System. <https://doi.org/10.17597/isas.darts/hyb2-00200>.
- Suzuki, H., Yamada, M., Kouyama, T., Tatsumi, E., Kameda, S., Honda, R., Sawada, H., Ogawa, N., Morota, T., Honda, C., et al., 2018. Initial inflight calibration for Hayabusa2 optical navigation camera (ONC) for science observations of asteroid Ryugu. *Icarus* 300, 341–359. <https://doi.org/10.1016/j.icarus.2017.09.011>.
- Tapley, B., Schutz, B., Born, G.H., 2004. *Statistical orbit determination*. Elsevier.
- Tatsumi, E., Domingue, D., Schröder, S., Yokota, Y., Kuroda, D., Ishiguro, M., Hasegawa, S., Hiroi, T., Honda, R., Hemmi, R., et al., 2020. Global photometric properties of (162173) Ryugu. *Astronomy & Astrophysics* 639, A83. <https://doi.org/10.1051/0004-6361/201937096>.
- Triggs, B., McLauchlan, P.F., Hartley, R.I., Fitzgibbon, A.W., 2000. Bundle adjustment—a modern synthesis, in: *Vision Algorithms: Theory and Practice*. International Workshop on Vision Algorithms Corfu, Greece, September 21–22, 1999 *Proceedings*, Springer. pp. 298–372.
- Tsuda, Y., Mori, O., Funase, R., Sawada, H., Yamamoto, T., Saiki, T., Endo, T., Kawaguchi, J., 2011. Flight status of IKAROS deep space solar sail demonstrator. *Acta astronautica* 69, 833–840. <https://doi.org/10.1016/j.actaastro.2011.06.005>.
- Tsuda, Y., Saiki, T., Terui, F., Nakazawa, S., Yoshikawa, M., Watanabe, S., Team, H.P., et al., 2020. Hayabusa2 mission status: Landing, roving and cratering on asteroid Ryugu. *Acta Astronautica* 171, 42–54. doi:10.1016/j.actaastro.2020.02.035.

- Van Wal, S., Yoshikawa, K., Tsuda, Y., 2019. Deployment analysis and trajectory reconstruction of MINERVA-II rovers on asteroid Ryugu, in: 29th AAS/AIAA Space Flight Mechanics Meeting. AAS 19–243.
- Villa, J., French, A., McMahon, J., Scheeres, D., Hockman, B., 2021. Gravity estimation at small bodies via optical tracking of hopping artificial probes, in: 2021 AAS/AIAA Astrodynamics Specialist Conference. AAS 21–785.
- Wada, K., Ishibashi, K., Kimura, H., Arakawa, M., Sawada, H., Ogawa, K., Shirai, K., Honda, R., Iijima, Y., Kadono, T., et al., 2021. Size of particles ejected from an artificial impact crater on asteroid 162173 Ryugu. *Astronomy & Astrophysics* 647, A43. <https://doi.org/10.1051/0004-6361/202039777>.
- Watanabe, S., Hirabayashi, M., Hirata, N., Hirata, N., Noguchi, R., Shimaki, Y., Ikeda, H., Tatsumi, E., Yoshikawa, M., Kikuchi, S., et al., 2019. Hayabusa2 arrives at the carbonaceous asteroid 162173 Ryugu—A spinning top-shaped rubble pile. *Science* 364, 268–272. <https://doi.org/10.1126/science.aav8032>.
- Werner, R.A., 1997. Spherical harmonic coefficients for the potential of a constant-density polyhedron. *Computers & Geosciences* 23, 1071–1077. [https://doi.org/10.1016/S0098-3004\(97\)00110-6](https://doi.org/10.1016/S0098-3004(97)00110-6).
- Wertz, J.R., 1978. *Spacecraft Attitude Determination and Control*. Kluwer Academic Publishers.
- Yada, T., Abe, M., Okada, T., Nakato, A., Yogata, K., Miyazaki, A., Hatakeda, K., Kumagai, K., Nishimura, M., Hitomi, Y., et al., 2022. Preliminary analysis of the Hayabusa2 samples returned from C-type asteroid Ryugu. *Nature Astronomy* 6, 214–220. <https://doi.org/10.1038/s41550-021-01550-6>.
- Yamamoto, K., Otsubo, T., Matsumoto, K., Noda, H., Namiki, N., Takeuchi, H., Ikeda, H., Yoshikawa, M., Yamamoto, Y., Senshu, H., et al., 2020. Dynamic precise orbit determination of Hayabusa2 using laser altimeter (LIDAR) and image tracking data sets. *Earth, Planets and Space* 72, 85. <https://doi.org/10.1186/s40623-020-01213-2>.
- Yoshimitsu, T., Kubota, T., 2020. Engineering challenges and results by MINERVA-II Asteroid Surface Rovers. *J. Robot. Soc. Japan* (in Japanese) 38, 754–761. <https://doi.org/10.7210/jrsj.38.754>.
- Yoshimitsu, T., Kubota, T., Tomiki, A., Yoshikawa, K., 2019. Operation Results of MINERVA-II Twin Rovers Onboard Hayabusa2 Asteroid Mission. In: 70th International Astronautical Congress. IAC-19, A3,4A,4.